Nuclear Science and Techniques (2024) 35:211
https://doi.org/10.1007/s41365-024-01584-1

Neutron skin and its effects in heavy-ion collisions

Meng-Qi Ding[1] · De-Qing Fang[1,2] · Yu-Gang Ma[1,2]

Received: 22 June 2024 / Revised: 5 August 2024 / Accepted: 7 August 2024 / Published online: 22 November 2024

Abstract
Neutron skin is an exotic phenomenon that occurs in unstable nuclei. In this study, the various effects of the neutron skin on nuclear reactions and their relationship with the properties of nuclear structures are reviewed. Based on numerous studies using theoretical models, strong correlations have been found between the neutron skin thickness and the neutron removal cross section, neutron/proton yield ratio, t/^{3}He yield ratio, neutron–proton momentum difference, isoscaling parameter, photon production, reaction cross sections for neutron-induced reactions, charge-changing cross-sectional differences of mirror nuclei, astrophysical S-factor, and other quantities in nuclear reactions induced by neutron-rich nuclei. Moreover, the relationships between the neutron skin thickness and certain properties of the nuclear structure, such as α-cluster formation, α decay, nuclear surface, nuclear temperature, and proton radii difference of mirror nuclei, have also been investigated. Furthermore, it has also been shown that the neutron skin plays a crucial role in relativistic heavy-ion collisions. Experimentally, an unstable nucleus with a neutron skin can be generated by radioactive nuclear beam facilities, and the thickness of the neutron skin can be extracted by measuring the sensitive probes, which further helps impose stringent constraints on the equation of state of asymmetric nuclear matter and the properties of neutron stars.

Keywords Neutron skin · Radioactive nuclear beam · Equation of state of asymmetric nuclear matter

1 Introduction

The atomic nucleus is the microscopic structure of matter consisting of a certain number of protons and neutrons. Theoretical predictions suggest that approximately 9000 nuclei may exist [1, 2]. To date, more than 3300 nuclei have been discovered, including 3340 nuclei in their ground state and 1938 excited isomers with half-lives longer than 100ns [3]. Except for the 339 naturally existing nuclei, the remainder were artificially created. There are only 289 naturally existing nuclei with isospin abundance data, which contain 254 stable nuclei and 35 long-lifetime radioactive nuclei [4]. Through numerous studies on stable nuclei, a relatively complete theory has been established in traditional nuclear physics. For example, the nuclear radius is proportional to $A^{1/3}$, where A denotes the mass number. The density distributions of neutrons and protons in the nucleus are similar. Furthermore, nucleons are distributed in orbitals with different energy levels according to the shell model. With the development of radioactive nuclear beam (RNB) experimental methods and the construction of a series of RNB facilities worldwide, the rapid extension of nuclear charts to drip lines has revealed various new phenomena and physics in the domain of nuclear physics, such as the neutron halo, neutron skin, multi-nucleon clusters, shell evolution, exotic decay modes, disappearance of normal magic numbers, and appearance of new magic numbers [2, 5–10].

Dedicated to Professor Wenqing Shen in honor of his 80th birthday.

This work is partially supported by the National Natural Science Foundation of China (Nos. 11925502, 11935001, 12347106, 11961141003, 12147101, and 11890714), the Strategic Priority Research Program of the Chinese Academy of Sciences (No. XDB34030000), and the National Key R&D Program of China (No. 2023YFA1606404).

✉ De-Qing Fang
dqfang@fudan.edu.cn

✉ Yu-Gang Ma
mayugang@fudan.edu.cn

[1] Key Laboratory of Nuclear Physics and Ion-Beam Application (MOE), Institute of Modern Physics, Fudan University, 200433 Shanghai, China

[2] Shanghai Research Center for Theoretical Nuclear Physics, NSFC and Fudan University, 200438 Shanghai, China

For neutron-rich systems, owing to the large asymmetry between the proton (p) and neutron (n) numbers (denoted as Z and N, respectively), these two types of fermions tend to decouple around the surface region of the nucleus, which is called the neutron skin. The thickness of the neutron skin is defined as the difference between the root-mean-square (RMS) radii of the neutron and proton, that is, $\langle r_n^2\rangle^{1/2} - \langle r_p^2\rangle^{1/2}$. The proton radius of a nucleus can be extracted with relatively high accuracy through electromagnetic interaction [11]; however, it is challenging to directly obtain a precise measurement of the neutron radius in experiments owing to the charge neutrality of neutrons. Thus far, various experimental methods have been proposed to measure the distribution of neutrons by strong or weak interaction probes, such as hadron scattering [12, 13], giant dipole resonance [14, 15], spin dipole resonance [16], and antiprotonic annihilation [17, 18]. However, the extracted results are usually model-dependent and vary greatly by different experimental analysis approaches [19]. Consequently, reliable probes for measuring the neutron skin thickness are expected to be developed, which will have great significance in nuclear physics and astrophysics.

The equation of state (EOS) of nuclear matter is a fundamental problem in nuclear physics and macroscopically reflects microscopic nuclear interactions. The EOS can be expressed as the binding energy per nucleon of nuclear matter as follows:

$$E(\rho,\delta) = E_0(\rho) + E_{\rm sym}(\rho)\delta^2 + O(\delta^4), \tag{1}$$

where ρ_n, ρ_p, and $\rho = \rho_n + \rho_p$ are the neutron, proton, and total densities, respectively; $\delta = (\rho_n - \rho_p)/\rho$ is the isospin asymmetry; $E_0(\rho) = E(\rho, \delta = 0)$ is the energy per nucleon of symmetric nuclear matter; and $E_{\rm sym}(\rho)$ is the nuclear symmetry energy described by

$$E_{\rm sym}(\rho) \equiv \frac{1}{2!}\frac{\partial^2 E(\rho,\delta)}{\partial\delta^2}\bigg|_{\delta=0}. \tag{2}$$

The properties of symmetric nuclear matter are relatively well determined, whereas the isovector part remains largely uncertain and has attracted widespread attention. Research on the isovector part will help improve our understanding of the properties of radioactive nuclei, nuclear astrophysics, and dynamical evolution in heavy-ion collisions [20–29]. The density dependence of the symmetry energy is a crucial topic that shows great uncertainty when different nuclear forces or interaction potentials (in theory) are adopted, which can be regarded as soft or stiff [30]. Around the saturation density ρ_0, $E_{\rm sym}(\rho)$ can be expanded as follows:

$$E_{\rm sym}(\rho) = E_{\rm sym}(\rho_0) + \frac{L}{3}\left(\frac{\rho-\rho_0}{\rho_0}\right) + \frac{K_{\rm sym}}{18}\left(\frac{\rho-\rho_0}{\rho_0}\right)^2 + \cdots, \tag{3}$$

where L and $K_{\rm sym}$ are the slope and curvature of the symmetry energy at the saturation density, respectively, and are defined as follows:

$$L \equiv 3\rho_0 \frac{\partial E_{\rm sym}(\rho)}{\partial\rho}\bigg|_{\rho=\rho_0}, \tag{4}$$

$$K_{\rm sym} \equiv 9\rho_0^2 \frac{\partial^2 E_{\rm sym}(\rho)}{\partial\rho^2}\bigg|_{\rho=\rho_0}. \tag{5}$$

These two characteristic parameters play a critical role in determining the EOS of asymmetric nuclear matter because they govern the behavior of symmetry energy at the subsaturation and oversaturation densities. Based on various nuclear models, such as Skyrme, Gogny, and covariant models of different nature, it has been demonstrated that the neutron skin thickness is related to $E_{\rm sym}(\rho_0)$, L, $K_{\rm sym}$, the ratio $L/E_{\rm sym}(\rho_0)$, $E_{\rm sym}(\rho_0)$–$a_{\rm sym}$ (where $a_{\rm sym}$ is the symmetry energy of finite nuclei), and the ratio $E_{\rm sym}(\rho_0)/Q$ (where Q is the surface stiffness coefficient) [31–37]. Moreover, Ref. [38] proposed that the neutron skin thickness of heavy nuclei can be effectively determined by the EOS at a subsaturation cross density $\rho_c \approx 0.11$ fm^{-3} rather than at $\rho_0 \approx 0.16$ fm^{-3}. As a result, good knowledge of the neutron skin thickness will assist in obtaining information on the symmetry energy and determining the form of the EOS.

Furthermore, neutron stars are extremely dense and compact stars composed primarily of neutrons. Despite differing by 18 orders of magnitude on a spatial scale, the neutron skin and neutron stars have similar structures that are closely linked by the EOS of nuclear matter. Detailed analyses have confirmed that some properties of neutron stars depend on the EOS; therefore, precise neutron skin thickness data will help constrain the specific properties of neutron stars. Neutron stars, with masses between those of a white dwarf and a black hole, are formed after a supernova explosion caused by gravitational collapse at the end of the evolution of a massive star. A neutron star is one of the densest forms of matter in the universe, whose mass is approximately 1.5 times that of the sun, and its radius is approximately 12 km [39]. The density inside a neutron star can reach or even exceed 5–6 times that of normal nuclear matter, which approximates that of the center of a heavy nucleus and is approximately 10^{14} times that of water. Generally, neutron stars consist of four major regions: the outer crust with nuclei and electron gas; the

inner crust with nuclei, neutrons, and electrons; the outer core with uniformly distributed electrically neutral nuclear matter; and the dense inner core, probably containing other particles such as hyperons and quarks. The first evidence of the existence of neutron stars was the discovery of pulsars in 1967. The detection of gravitational waves from a binary neutron star merger (GW170817) by the LIGO-Virgo Collaboration [40] opened a new era of multi-messenger astronomy and highlighted the importance of astrophysics in exploring the nature of dense matter and the synthesis of heavy elements. There is no direct connection between the neutron skin and the neutron stars; however, they are linked by the EOS of the nuclear matter. The slope of the symmetry energy corresponds to the pressure of the nuclear matter, which is closely related to both the neutron skin thickness and the radii of neutron stars. The relationship between neutron skin thickness and neutron star properties helps us understand the EOS of nuclear matter more comprehensively as well as provides opportunities to study the properties of neutron stars in the laboratory. The dependences of the neutron skin thickness or EOS on the properties of neutron stars have been extensively studied, such as the mass–radius relation [41–43], crust–core transition [44–47], onset of the direct Urca process [48, 49], and stellar moment of inertia [50, 51]. For example, the K_{sym}–L correlation significantly influences the crust–core transition, radius, and tidal deformability of canonical neutron stars, particularly at small L values [52]. With a variety of interactions or theoretical models, different EOS correspond to different mass–radius relationships of the neutron star [53]. In addition, Ref. [54] provided an upper limit on the neutron skin thickness of ^{208}Pb based on the GW170817 data and, conversely, provided a lower limit on the tidal polarizability by relying on the lower limit of the measured neutron skin thickness of ^{208}Pb via parity-violating electron nucleus scattering, which can further infer the properties of the EOS [54]. Furthermore, Ref. [55] discussed the influence of the neutron skin, isospin diffusion, tidal deformability, and maximum mass of a neutron star on the constraints of the symmetry energy and its associated nuclear matter parameters. Although correlations between neutron skin thickness and several neutron star observables have been proven to exist in several studies, these results have some system dependence and uncertainty. To describe the degree of correlation between various observables quantitatively, Ref. [56] developed a covariance analysis to quantify the theoretical errors and correlation coefficients. Recently, statistical analyses were performed on the cores of neutron stars in the crust. For example, using pure neutron matter and neutron skin data, a Bayesian inference of neutron star crust properties is presented in Ref. [57] based on a compressible liquid drop model with an extended Skyrme energy density functional (EDF), such as the crust–core transition pressure, crust–core transition baryon chemical potential, and thickness of the pasta phases relative to the crust.

In this study, a comprehensive review of the effects of the neutron skin on nuclear reactions is presented. The remainder of this paper is organized as follows: in Sect. 2, previous studies on the effects of the neutron skin in nuclear reactions using diverse theoretical or phenomenological approaches are briefly presented. In Sect. 3, recent progress on neutron skin effects in the studies on relativistic heavy-ion collisions is discussed. In Sect. 4, experimental detection methods for the neutron skin are introduced. Finally, in Sect. 5, the conclusions of this study are presented.

2 Effects of neutron skin in nuclear reactions

Compared with stable nuclei, nuclei with a neutron skin exhibit unique structural characteristics, and the density distributions of neutrons are more extended than those of protons, leading to various effects in nuclear reactions. In this review, the correlations between the neutron skin and several parameters are introduced: (A) neutron removal cross section, (B) yield ratios of light particles (neutron/proton; triton/^{3}He), (C) momentum difference between neutrons and protons, (D) projectile fragmentation, (E) photon emission, (F) reaction cross sections for nucleon-induced reactions, (G) properties of the nuclear structure (α-cluster formation, α-decay half-life, nuclear surface, and nuclear temperature), (H) properties of mirror nuclei (proton RMS radii difference of mirror nuclei, charge-changing cross-sectional difference of mirror nuclei), and (I) astrophysical S-factor.

2.1 Neutron skin and neutron removal cross section

A statistical abrasion ablation (SAA) model was developed to describe heavy-ion collisions by considering nuclear reactions as a two-step process: abrasion and evaporation. This model considers the neutron and proton density distributions separately and provides complete statistics of nucleon–nucleon collisions in the overlapping region of the two colliding nuclei, which can effectively describe the fluctuation of the neutron-to-proton ratio in the process of fragmentation and to study the isospin effect in nuclear reactions [58]. Based on the SAA model, the relationship between neutron skin thickness and neutron removal cross section (σ_{-N}) has been studied in Refs. [59, 60]. Different neutron skin sizes were obtained by adjusting the diffuseness parameter of the neutrons in the two-parameter Fermi distribution. The neutron removal cross section is defined as the summation of production cross sections for fragments with

the same proton number as the projectile but with a smaller neutron number. Previous studies have confirmed that there is a strong correlation between neutron skin thickness and neutron removal cross section [59]. Similarly, the proton removal cross section (σ_{-p}) is defined as the summation of production cross sections for fragments with the same neutron number as the projectile. As illustrated in Fig. 1, with an increase in the neutron skin thickness, the proton removal cross section decreases, which displays the opposite dependence compared with the neutron removal cross section [60]. This reveals that, for nuclei with a large neutron skin, the neutrons have a more expanded spatial distribution than protons such that the neutrons may be easier to remove in peripheral collisions. Furthermore, to eliminate the systematic measurement error in the experiments, the ratio between the (one-)neutron and proton removal cross section is also explored, which is found to be proportional to the neutron skin thickness and is a more sensitive probe for determining the neutron skin thickness. Moreover, Ref. [61] demonstrated that the neutron removal cross section is sensitive to the neutron skin thickness for Sn isotopes, as calculated by the relativistic mean-field theory based on variations of the DD2 interaction, which potentially provides constraints on the symmetry energy.

2.2 Neutron skin and yield ratios of light particles

The isospin-dependent quantum molecular dynamics (IQMD) model is a semiclassical microscopic transport theory developed from the traditional QMD model by appropriately considering the isospin degrees of freedom, which provides reasonable explanations for the nuclear reactions induced by nuclei far from the β-stability line [62–75]. In this model, each nucleon is regarded as a Gaussian wave packet with a finite width instead of a classical point particle, and three basic components of dynamics in intermediate-energy heavy-ion collisions are involved: mean field, two-body collisions, and Pauli blocking. Within the framework of the IQMD model, the collision processes of Ca and Ni isotopes with a ^{12}C target at an incident energy of 50 MeV/nucleon were simulated to investigate the dependence between the neutron skin thickness and the yield ratio of the emitted neutrons and protons [R(n/p)] in Refs. [76, 77]. The neutron and proton density distributions used for the phase-space initialization in the IQMD model originate from the droplet model, which can obtain different values of neutron skin thickness by changing the diffuseness parameter of the neutron density for the neutron-rich projectile. With different impact parameters, it was found that, from central to peripheral collisions, the neutron skin thickness is always proportional to R(n/p), which is the most sensitive in peripheral collisions because the difference in density distributions between neutrons and protons is primarily reflected in the surface region of neutron-rich nuclei. In addition, Ref. [78] suggested that the effects of neutron skin thickness on R(n/p) are more prominent at a lower momentum. Therefore, R(n/p) can be considered an experimentally observable parameter for extracting the neutron skin thickness. Nevertheless, the precise measurement of R(n/p) is possible in experiments owing to the low detection efficiency for neutrons. Hence, Ref. [79] explored relatively heavier charged particles such as tritons and ^{3}He, which are considerably easier to measure experimentally. Figure 2 shows that there is a linear correlation between the neutron skin thickness and the yield ratio of triton to ^{3}He [R(t/^{3}He)]. For different neutron skin thicknesses, R(t/^{3}He) is proportional to R(n/p), that is, the double ratio R(t/^{3}He)/R(n/p) is almost constant. Consequently, both R(n/p) and R(t/^{3}He) can be used as possible experimental probes for measuring the neutron skin thickness, as reported in Refs. [78, 80, 81]. However, R(t/^{3}He) can provide higher precision in measuring the neutron skin thickness because the yields of charged particles can be measured accurately.

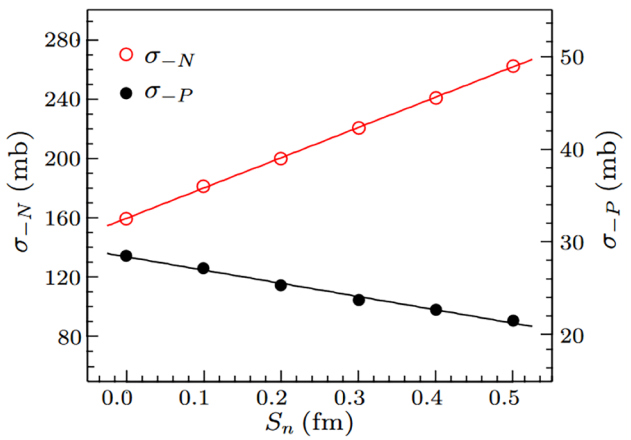

Fig. 1 (Color online) Correlation among the neutron removal cross section (left Y axis), proton removal cross section (right Y axis), and neutron skin thickness for ^{48}Ca + ^{12}C reactions at 100 MeV/nucleon [60]

2.3 Neutron skin and the difference of momentum between neutrons and protons

In terms of wave functions in quantum mechanics, the density and momentum distributions are the Fourier transforms of each other. According to the uncertainty principle, smaller intrinsic momentum fluctuations between fragments imply greater dispersion in coordinate space. It is easier to measure the momentum than the density distribution of neutrons in experiments. Therefore, using the IQMD model, Ref. [78] studied the dependence of the difference in momentum between neutrons and protons on the neutron skin thickness by simulating the semi-peripheral collisions

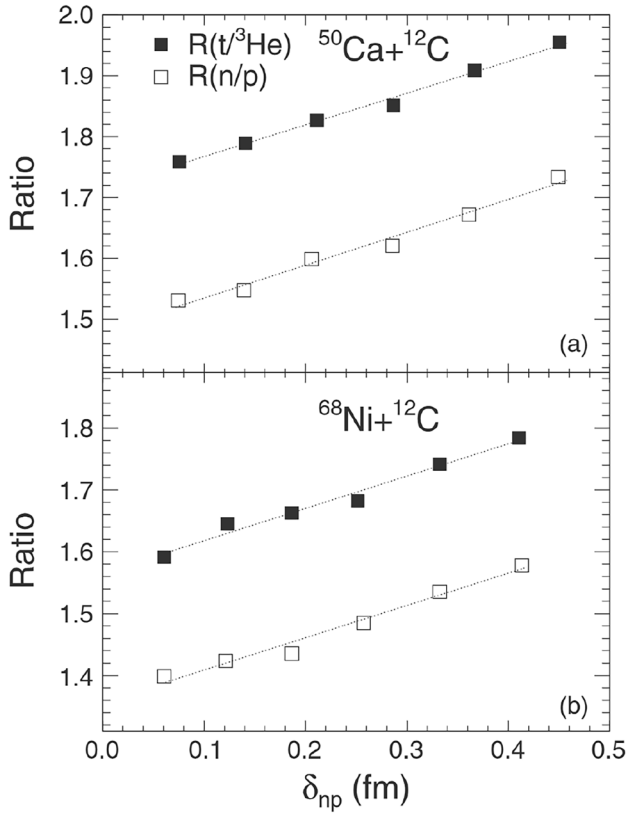

Fig. 2 (Color online) Correlation among the neutron-to-proton yield ratio, triton-to-^{3}He yield ratio, and neutron skin thickness for ^{50}Ca + ^{12}C (**a**) and ^{68}Ni + ^{12}C (**b**) at 50 MeV/nucleon [79]

of neutron-rich Ca, Mg, and Ne isotopes on the ^{12}C target at 50 MeV/nucleon. The difference in momentum between neutrons and protons is defined as the average magnitude of the relative momentum for every possible permutation and combination. It was found that the neutron–proton momentum difference decreased linearly with increasing neutron skin thickness in both the initial and final states, as illustrated in Fig. 3. This means that, if neutrons and protons become closer in space distribution, they will have a larger difference in momentum distribution. Further study showed that the normalized momentum spectra of emitted neutrons are distinct for different neutron skin thicknesses, whereas those of protons are almost the same. With a thicker neutron skin, the peak position of the momentum spectrum of neutrons is smaller, indicating that the average momentum of emitted neutrons decreases. Furthermore, the difference in momentum between tritons and ^{3}He can be used as a probe for measuring the neutron skin thickness of a nucleus with large isospin asymmetry, such as ^{60}Ca, ^{37}Mg, and ^{31}Ne. With the development of detector technology, the detection efficiency of neutrons has improved, making it possible to extract useful information regarding neutron skin thickness

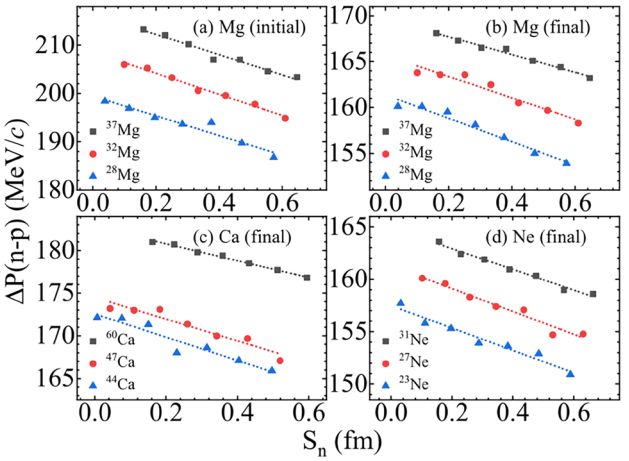

Fig. 3 (Color online) Correlation between the neutron–proton momentum difference and neutron skin thickness for ^{28,32,37}Mg + ^{12}C in the initial state (**a**), ^{28,32,37}Mg + ^{12}C in the final state (**b**), ^{44,47,60}Ca + ^{12}C in the final state (**c**), and ^{23,27,31}Ne + ^{12}C in the final state (**d**) at 50 MeV/nucleon [78]

from the neutron–proton momentum difference in future experiments.

2.4 Neutron skin and projectile fragmentation

Projectile fragmentation is a well-established technique for producing rare isotopes by bombarding a projectile nucleus on the target nucleus with a certain incident energy. It can produce a variety of fragments with a wide mass region from nucleons to heavy fragments and a wide isospin region from neutron-deficient to neutron-rich isotopes [82–84]. This process can be explained well by the participant–spectator model [85]. In a peripheral collision, the overlap zone between the projectile and the target (called the participant) leads to the abrasion and evaporation of nucleons or light fragments, whereas the residues with a charge number close to that of the projectile (called the spectator or projectile-like fragments) fly away at a nearly unchanged velocity, which may retain significant information about the initial density distribution of the projectile. Therefore, some observables in projectile fragmentation have been studied for their relevance to the neutron skin, which is conducive to extracting useful information on the nuclear structure and EOS of asymmetric nuclear matter as well as the reaction mechanism of nuclear collisions.

The isoscaling phenomenon is a fascinating topic in the survey of isospin effects in fragmentation dynamics and has been observed in both theoretical and experimental studies. Based on two similar nuclear reactions that differ only in isospin asymmetry, it was found that the yield ratio of a given isotope in the two reactions (denoted as 1 and 2, respectively) obeys the scaling law and has exponential

dependencies on neutron and proton numbers, which can be expressed as follows:

$$R_{21}(N,Z) = Y_2(N,Z)/Y_1(N,Z) = C\exp(\alpha N + \beta Z), \quad (6)$$

where α and β are the isoscaling parameters and C is a normalization constant [86]. In the grand-canonical approximation, α and β are equal to the difference in the chemical potentials between the two reaction systems for neutrons and protons, respectively. Systematical isoscaling analyses were performed on light fragments with $Z \leq 8$, and the results demonstrated that the isoscaling parameters remained constant for different fragments and had a linear dependence on the symmetry energy, making it feasible to indirectly determine the symmetry energy term of the EOS. Therefore, the isoscaling behavior of heavy fragments would also be of considerable interest. Ref. [87] investigated the sensitivity of isoscaling behavior to the neutron skin thickness for projectile-like fragments by simulating the peripheral collisions of ^{50}Ca + ^{12}C and ^{48}Ca + ^{12}C at 50 MeV/nucleon through the IQMD model followed by the GEMINI decay code. Figure 4 shows that, with an increase in the neutron skin thickness of ^{50}Ca, the extracted isoscaling parameter α decreases linearly. In addition, under the same neutron skin thickness, α is not a constant for heavy fragments with different proton numbers, which exhibit different isoscaling behaviors from light particles, probably originating from different formation mechanisms. Moreover, the average value of N/Z of projectile-like fragments exhibited a negative linear relationship with the neutron skin thickness. Consequently, the experimental measurements of both the isoscaling parameter α and the mean N/Z of projectile-like fragments can be included in the valuable evaluation of the neutron skin thickness to further set stringent constraints on the critical parameters of the EOS. However, a distortion of the isoscaling phenomenon was found in Ref.[88]. Based on the experimental data and two different theoretical models, Ref.[88] examined the isoscaling properties of neutron-rich fragments produced in highly asymmetric systems, such as ^{40,48}Ca + ^{9}Be and ^{58,64}Ni + ^{9}Be, at 140 MeV/nucleon. They reported that the isoscaling law is obeyed when the fragments have the same range of neutron excess $I = N - Z$. This means that the fragments share the same environment, that is, the same collision region, temperature, and nuclear density. Additionally, the correlation between $|\beta|$ and α varies for fragments with different I values, indicating that the $|\beta|/\alpha$ ratio for a specific fragment can be adopted to detect differences in neutron and proton densities in different regions of the nucleus.

Recently, Ref. [89] studied the parallel momentum distribution ($p_{\parallel}$) of residual fragments by simulating the ^{48}Ca + ^{9}Be projectile fragmentation reaction at 140 MeV/nucleon within the framework of the Lanzhou QMD (LQMD) model, which is an isospin- and momentum-dependent transport model. The initial density distribution adopts a Fermi distribution with two parameters. The $p_{\parallel}$ is nonsymmetric and can be fitted using a combined Gaussian function, resulting in different width parameters for the left (Γ_L) and right sides (Γ_R) of the distribution. The results confirmed that the Γ_L of projectile-like fragments in peripheral collisions is sensitive to the neutron skin thickness of the neutron-rich projectile nucleus, as shown in Fig. 5. The $p_{\parallel}$ is easily measured in experiments; therefore, Γ_L of $p_{\parallel}$ can serve as a possible probe for measuring the neutron skin thickness.

Furthermore, the effect of the neutron skin on the cross sections of primary projectile-like residues is presented in Ref. [90]. The collisions of ^{124,132}Sn + ^{124}Sn at 200 MeV/nucleon were calculated by developing a new version of an improved QMD (ImQMD-L) model, in which the neutron skin of the nuclei in the initialization and the mean-field potential in nucleon propagation are consistently considered. The neutron skin thickness was altered by employing five sets of Skyrme parameters corresponding to different values of the slope of the symmetry

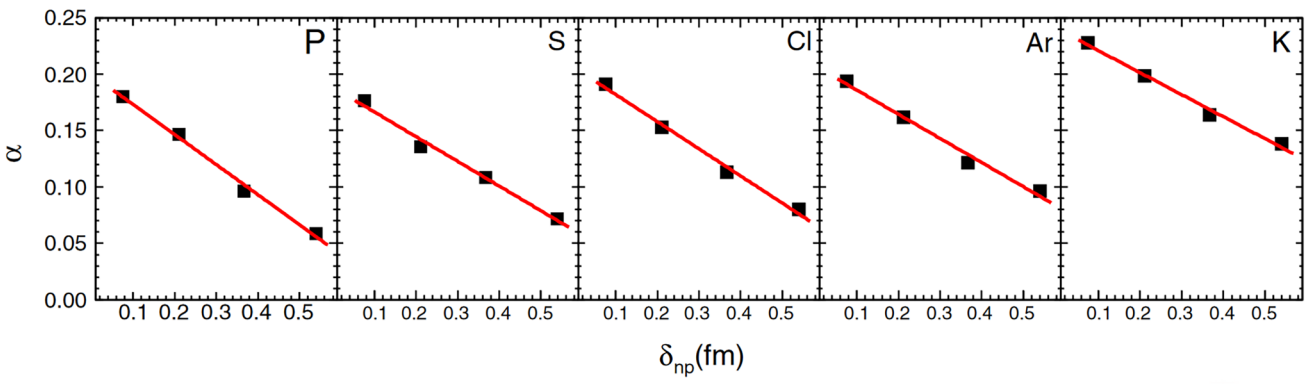

Fig. 4 (Color online) Correlation between the isoscaling parameter α and the neutron skin thickness for fragments with the proton number varying between 15 and 19 based on the two reactions ^{50}Ca + ^{12}C and ^{48}Ca + ^{12}C at 50 MeV/nucleon [87]

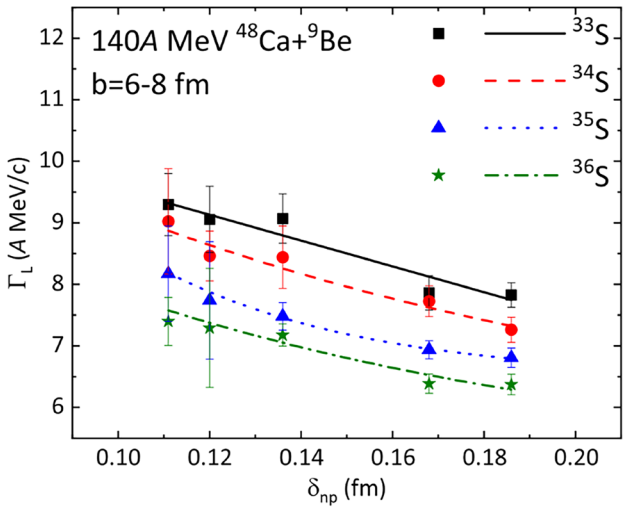

Fig. 5 (Color online) Correlation between the width of the left side of the parallel momentum distribution for neutron-rich sulfur fragments and the neutron skin thickness of ^{48}Ca for ^{48}Ca + ^{9}Be at 140 MeV/nucleon. [89]

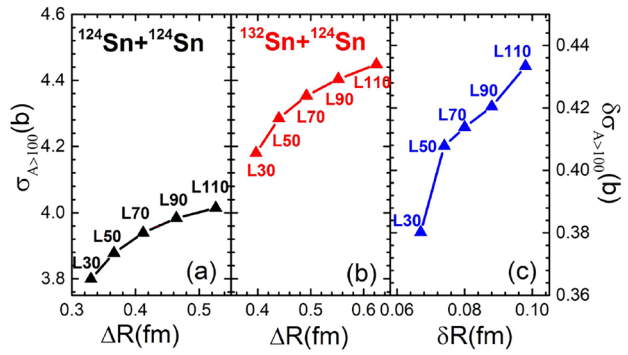

Fig. 6 (Color online) Correlation between the cross sections of the projectile-like residues with $A > 100$ and the neutron skin thickness for ^{124}Sn + ^{124}Sn (**a**) and ^{132}Sn + ^{124}Sn (**b**) at 200 MeV/nucleon. Correlation between the difference of $\sigma_{A>100}$ and that of neutron skin thickness between the two systems (**c**) [90]

energy, varying from 30MeV to 110MeV. As shown in Fig. 6a and b, the cross sections of primary projectile-like residues with a mass number $A > 100$ ($\sigma_{A>100}$) positively correlated with the neutron skin thickness and the slope of the symmetry energy for both systems. To suppress the systematic uncertainty caused by the model, the difference in $\sigma_{A>100}$ between the two systems ($\delta\sigma_{A>100}$) was further investigated, and the results confirmed that $\delta\sigma_{A>100}$ is still associated with the difference in the neutron skin thickness between the two systems and the slope of the symmetry energy (see Fig. 6c). Thus, it is possible to use $\sigma_{A>100}$ or $\delta\sigma_{A>100}$ as experimental probes for determining the neutron skin thickness of unstable nuclei and constraining the symmetry energy.

Other observables of the fragmentation reactions were studied in Ref. [91], including the neutron removal, charge-changing, and total interaction cross sections. The results indicated that these quantities are dependent on the neutron skin thickness. This can be used to provide constraints on the slope of the symmetry energy as well as a better understanding of the properties of neutron stars. For example, Fig. 7 illustrates that the charge-changing cross sections tend to increase linearly with increasing isospin asymmetry, that is, larger neutron skin sizes of the projectile. Furthermore, configurational information entropy (CIE) analysis was adopted to conclude that the related CIE quantities, for example, the isotopic/mass/charge cross-sectional distributions, in projectile fragmentation reactions are sensitive to the neutron skin thickness of neutron-rich nuclei [92, 93].

2.5 Neutron skin and photon emission

Compared with conventional hadronic probes, photons interact weakly with the nuclear medium and only through electromagnetic interactions [94, 95]. Hence, they are not interfered with by final-state interactions; therefore, a more realistic picture of nuclear matter can be obtained. Both the theoretical and experimental results have demonstrated that hard photons, that is, photons with energies greater than 30MeV, primarily originate from incoherent proton–neutron bremsstrahlung collisions in intermediate-energy heavy-ion collisions. These photons are emitted from two distinct sources: direct and thermal hard photons. Direct hard photons are derived from an earlier stage of the reaction, which may preserve the memory of the initial projectile. Ref. [96]

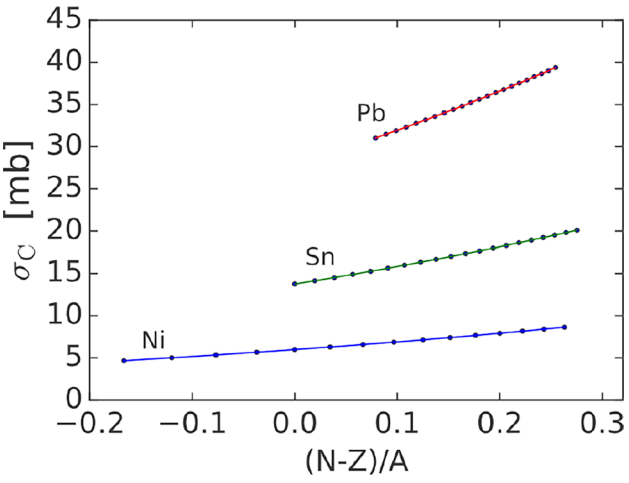

Fig. 7 (Color online) Correlation between charge-changing cross sections and isospin asymmetry of the projectiles for Ni, Sn, and Pb isotopes on C targets at 1GeV/nucleon [91]

explored the effects of neutron skin on direct hard photon emission from the reactions of ^{50}Ca + ^{12}C and ^{50}Ca + ^{40}Ca within the framework of the IQMD model, wherein the channel of incoherent proton–neutron bremsstrahlung collisions is embedded. The results showed that more direct hard photons were produced in the peripheral collisions for thicker neutron skins. Moreover, it was confirmed that the yield ratio of direct hard photons between the central and peripheral collisions in the same reaction system [$R_{\rm cp}(\sigma_\gamma)$] shows a decreasing trend with an increase in the neutron skin thickness, which is more sensitive at higher incident energies. They concluded that the neutron skin has a significant effect on the rapidity dependence of multiplicity (N_γ) and the multiplicity ratio between the central and peripheral collisions [$R_{\rm cp}(N_\gamma)$] for direct hard photons. With an increase in the neutron skin thickness, N_γ tends to increase, whereas $R_{\rm cp}(N_\gamma)$ decreases. In addition, the rapidity dependence of $R_{\rm cp}(N_\gamma)$ exhibits different behaviors in the two reaction systems. By adjusting the neutron skin thickness of the projectile ^{50}Ca, the largest difference in the rapidity distribution of $R_{\rm cp}(N_\gamma)$ appeared near the target nucleus side for the target ^{12}C while at approximately zero rapidity for the target ^{40}Ca, which is a more symmetric system. Therefore, direct hard photon emission can be used as an experimental observable to extract information on the neutron skin thickness and is significantly cleaner than the abovementioned probes, such as nucleons, light fragments, and projectile-like fragments produced in the reaction. Refs. [97, 98] also demonstrated that the production of hard photons is sensitive to neutron skin thickness. Further theoretical research is necessary to explore the dependence of the direct hard photon emission on the EOS and symmetry energy.

2.6 Neutron skin and reaction cross sections for nucleon-induced reactions

The isospin effects in the proton (neutron)-induced reactions of Sn isotopes at 100MeV were investigated in Ref. [99] using the ImQMD model. The reaction cross sections for nucleon-induced reactions are influenced by both the neutron skin thickness of the target nuclei combined with the isospin dependence of the nucleon–nucleon cross sections and the motion of the incident nucleon from the nuclear mean field. The effects of density dependence of the symmetry energy on nucleon-induced reactions were systematically studied in Ref. [100]. Ref. [99] further attempted to disentangle the effects of neutron skin thickness and symmetry potential. They artificially created two sets of initial nuclei with different neutron skin thicknesses and correct binding energies. The results indicated that the reaction cross sections for proton-induced reactions were sensitive to the density dependence of the symmetry energy but less sensitive to the neutron skin thickness of the target nuclei, whereas neutron-induced reactions exhibited opposite effects. Therefore, the reaction cross sections of neutron-induced reactions are less sensitive to the density dependence of symmetry energy but sensitive to the neutron skin thickness of the target nuclei, which potentially provides an approach to obtaining information on the neutron skin thickness.

2.7 Neutron skin and properties of the nuclear structure

Owing to the structural particularity of the neutron skin, several characteristics of the nuclear structure may be used as potential probes for measuring the neutron skin thickness. Theoretical studies have suggested that the formation of α clusters in heavy nuclei is closely related to the properties of α decay [101, 102] and has a certain probability of occurring at the very surface of the nucleus in the ground state [103–105]. The surface α-clustering phenomenon also appears in neutron-rich heavy nuclei, leading to a tight connection between α-cluster formation and neutron skin thickness. This implies that the growth of the neutron skin suppresses the α cluster at the nuclear surface [103, 106, 107]. This has been experimentally confirmed by the monotonous reduction of the proton-induced α-knockout reaction (p, pα) cross section with increasing mass number for neutron-rich Sn isotopes [108]. Recently, a negative correlation between neutron skin thickness and α clustering in C isotopes was verified within the framework of antisymmetrized molecular dynamics [109]. In addition, in the α decay of heavy nuclei, the influence of the neutron skin thickness on the α-decay half-life was explored in Refs. [110–113]. For instance, using a generalized density-dependent cluster model, Ref. [113] suggested a negative linear correlation between the calculated α-decay half-life and the neutron skin thickness of daughter nuclei, as displayed in Fig. 8. This implies that an increase in the neutron skin thickness hinders α decay.

Theoretically, it is expected that the difference between proton and neutron surface widths is of great significance in determining the neutron skin thickness [116]. An appropriate correction of the nuclear surface diffuseness to the neutron skin thickness was applied in the macroscopic model, that is, a compressible droplet model, in which the nuclear density distribution followed the Fermi distribution with two parameters [116]. The deduced macroscopical neutron skin thicknesses were compared with the results calculated using a microscopic Skyrme–Hartree–Fock (SHF)+ Bardeen–Cooper–Schrieffer (BCS) method with several sets of Skyrme effective interactions. The results confirmed that there is an obvious dependence between the surface widths and the neutron skin thickness.

The temperature dependence of the neutron skin was analyzed in Ref. [117] using the finite-temperature SHF+BCS

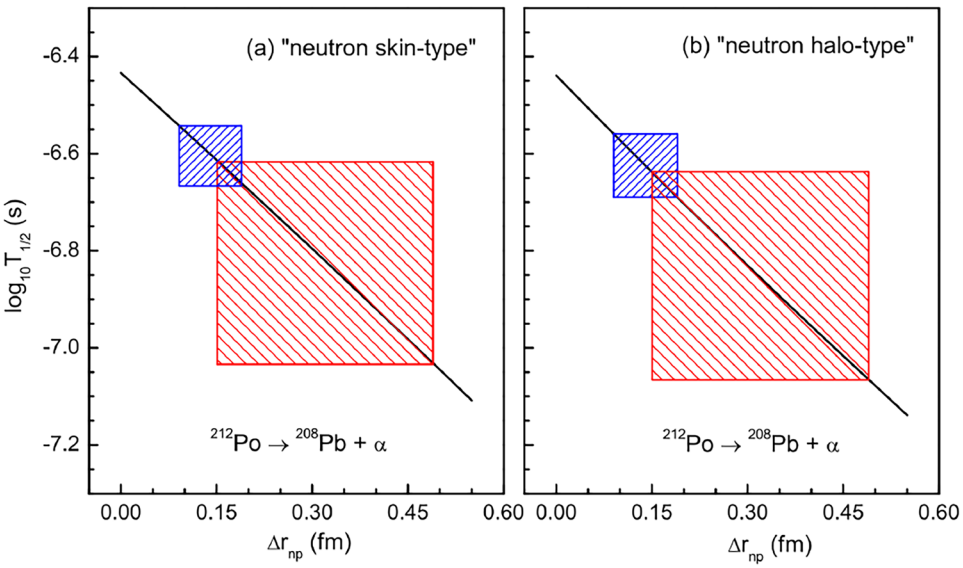

Fig. 8 (Color online) Correlation between the theoretical α -decay half-life of the parent nucleus ^{212}Po and the neutron skin thickness of the daughter nucleus ^{208}Pb with "neutron skin–type" (**a**) and "neutron halo–type" distributions (**b**). The red and blue zones correspond to the neutron skin thickness deduced from parity-violating electron scattering [114] and coherent pion photoproduction cross sections [115], respectively [113]

approximation. It is known that at the critical temperature, the pairing correlations disappear and a phase change from the superfluid to the normal state is observed. The study discovered that the proton radius of ^{120}Sn remained constant up to the critical temperature, whereas the neutron radius slightly decreased. However, there was an increasing trend in both the proton and neutron radii above the critical temperature. Hence, with an increase in temperature, the neutron skin thickness first decreases slightly and then increases substantially, reaching a minimum value at the critical temperature. The effect of the *N*/*Z* value on the temperature dependence of the neutron skin in the Sn isotopic chain was further investigated [117]. It has been demonstrated that an increase in the proton radius hinders the formation of neutron skin in less-neutron-rich nuclei. These results may be attributed to the effect of temperature on the occupation probabilities of single-particle states around the Fermi level.

2.8 Neutron skin and properties of mirror nuclei

Mirror nuclei are nuclei with the same mass number but interchanged proton and neutron numbers. Assuming a perfect charge symmetry, the neutron radius of a given nucleus is strictly equal to the proton radius of the corresponding mirror nucleus; therefore, the neutron skin thickness can be evaluated through the difference in the proton RMS radius of the mirror nuclei ($R_{\rm p}^{\rm mir}$). Although the charge symmetry is slightly broken in reality because of the Coulomb interaction, a linear relationship between the difference in the RMS charge radii of mirror nuclei and $|N-Z|\times L$ has been theoretically predicted to exist [118, 119]. A previous study has shown that the neutron skin thickness is correlated with both $|N-Z|\times L$ and $E_{\rm sym}(\rho = 0.10\ {\rm fm}^{-3})$ [118]. Successive studies have been performed to investigate the effects of other factors on the abovementioned relationships such as pairing correlations, low-lying proton continuum, and deformation [120–122]. In Ref. [122], through systematical investigations using an axially deformed solution of the SHF–Bogoliubov equations with 132 sets of Skyrme interaction parameters, the neutron skin thickness was demonstrated to be proportional to $R_{\rm p}^{\rm mir}$, even when considering the Coulomb interaction, as shown in Fig. 9. Moreover, the pairing effects can enhance the correlation for most mirror pairs, whereas the deformation effects may weaken the correlation when compared with the results of the SHF model. Based on the experimental value of $R_{\rm p}^{\rm mir}$, it is possible to deduce

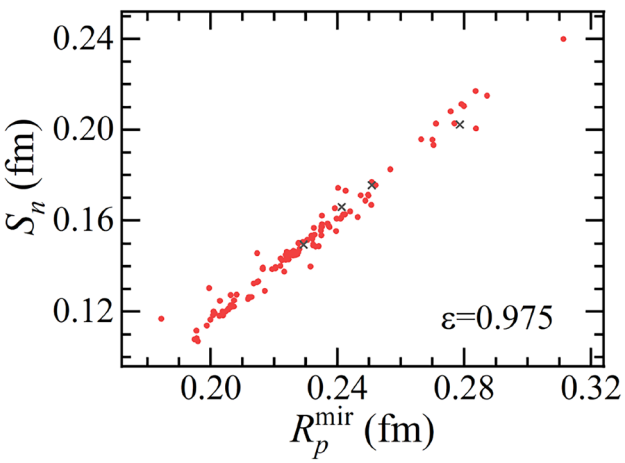

Fig. 9 (Color online) Correlation between the difference of the proton radii of mirror nuclei and the neutron skin thickness for the ^{48}Ca – ^{48}Ni pair. ε is the coefficient of determination of the linear fit [122]

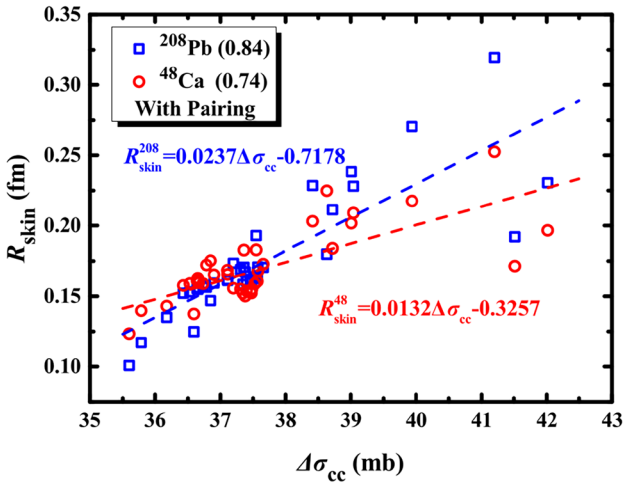

Fig. 10 (Color online) Correlation between the difference of the charge-changing cross section of mirror nuclei ^{30}Si − ^{30}S and the neutron skin thickness of ^{208}Pb and ^{48}Ca. The numbers in parentheses are the coefficients of determination of the linear fit [127]

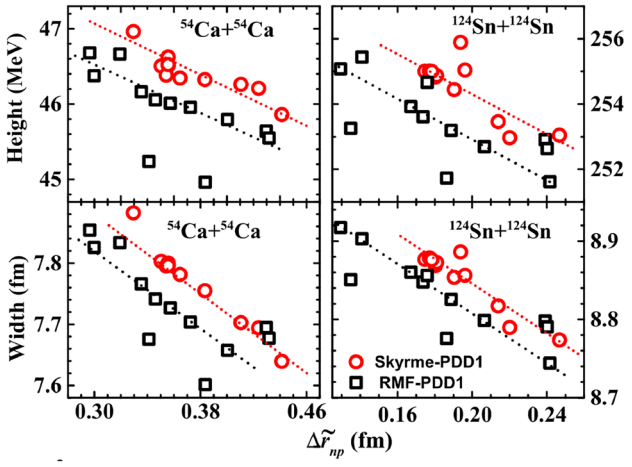

Fig. 11 (Color online) Correlation between the barrier parameters (heights and widths) and the neutron skin thickness [135]

the neutron skin thickness of neutron-rich nuclei and constrain the range of L. In addition, it was found that the neutron skin thickness of a neutron-rich nucleus is also approximately proportional to R_p^{mir} of its isotones, and the linearity is stronger with a larger $|N-Z|$ [122]. This provides an approach to determine the neutron skin thickness of an unstable nucleus even without experimental R_p^{mir} data.

In addition, recent studies indicate that the precise measurement of the charge-changing cross section (σ_{cc}) could be a novel and valid method for extracting the charge radii of unstable nuclei [123–126]. Therefore, the relationship between the charge-changing cross-sectional difference of mirror nuclei ($\Delta\sigma_{cc}$) and L or the neutron skin thickness has been further investigated [127]. Using both the SHF theory and covariant (relativistic) density functionals together with a Glauber model analysis, it was found that σ_{cc} is perfectly proportional to proton RMS radii and that L demonstrates a good linear correlation with $\Delta\sigma_{cc}$, R_p^{mir}, or neutron skin thickness for the ^{30}Si − ^{30}S pair [127]. Furthermore, Fig. 10 shows that the $\Delta\sigma_{cc}$ of ^{30}Si − ^{30}S mirror nuclei is sensitive to the neutron skin thickness of both ^{48}Ca and ^{208}Pb, meaning that the light mirror nuclei can be used to constrain the EOS, which can be implemented more simply with the currently available experimental facilities. Consequently, the charge-changing cross-sectional difference of the mirror nuclei is expected to be an effective surrogate for probing the neutron skin thickness or density dependence of the symmetry energy.

2.9 Neutron skin and astrophysical *S*-factor

The density dependence of the symmetry energy and the properties of the neutron skin are of vital importance in several domains, ranging from nuclear physics to astrophysics [46, 128–132]. Heavy-ion fusion reactions at low incident energies are governed by quantum tunneling through the Coulomb barrier, which is formed by repulsive long-range Coulombs and attractive short-range nuclear interactions [133, 134]. The behavior of sub-barrier fusion reactions is a critical issue in the formation of superheavy elements as well as in nuclear astrophysics. The cross section can be expressed as follows:

$$\sigma(E) = E^{-1}\exp(-2\pi\eta)S(E), \tag{7}$$

where E is the center of mass energy of the reaction system; η is the Sommmerfeld parameter; and $S(E)$ is the astrophysical S-factor, which varies weakly with energy and includes the effects of the nuclear structure. Reference [135] explored the sensitivity of neutron skin thickness to the astrophysical S-factor for heavy-ion fusion cross sections. The nucleus–nucleus potentials were generated from the double-folding model, where the density distributions of nucleons as key inputs were calculated by different families of non-relativistic and relativistic mean-field models corresponding to a wide range of neutron skin thicknesses or L. As shown in Fig. 11, the barrier parameters, such as its height and width, decreased with increasing neutron skin thickness, which led to the enhancement of the cross section and astrophysical S-factor up to one or two orders of magnitude. Moreover, Fig. 12 clearly illustrates that the S-factor is approximately proportional to the neutron skin thickness. The results from various asymmetric systems showed that

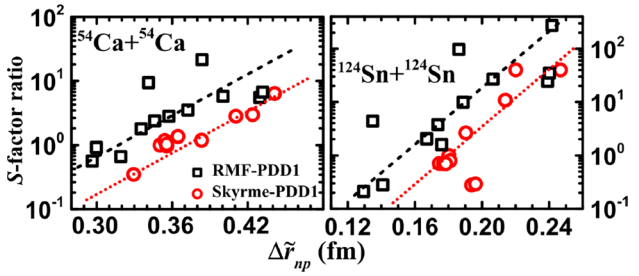

Fig. 12 (Color online) Correlation between *S*-factor ratio and neutron skin thickness [135]

these effects became stronger with increasing proton numbers. Therefore, it may be possible to determine the neutron skin thickness or L from the precise measurement of the sub-barrier fusion cross section or the astrophysical S-factor.

3 Neutron skin and high-energy heavy-ion collisions

Relativistic heavy-ion collisions are crucial in nuclear physics, which aims to investigate the properties of hot dense matter, known as quark-gluon plasma (QGP) [136–147]. Recently, extensive attention has been paid to the effects of exotic nuclear structures, such as the neutron skin and deformation, on the final observables in relativistic heavy-ion collisions [148, 149]. The relevant simulations were performed based on isobaric $^{96}_{44}$Ru + $^{96}_{44}$Ru and $^{96}_{40}$Zr + $^{96}_{40}$Zr collisions at ultra-relativistic energies [150, 151]. Specifically, in Ref. [152], different neutron skin sizes were calculated using two EDF theories, namely, the standard and extended SHF, with various symmetry energy parameters. Using the four dynamic models (AMPT-sm, UrQMD, HIJING, AMPT-def) and two static models (TRENTO and Glauber), it was found that the charged hadron multiplicity (N_{ch}) difference between the two isobaric collisions is sensitive to the neutron skin thickness, which is weakly model-dependent, as shown in Fig. 13. Furthermore, Refs. [153, 154] showed that the neutron skin thickness is closely related not only to the yield ratio of free spectator neutrons produced in high-energy isobaric collisions but also to the yield ratio of free spectator neutrons to protons in a single collision system. In addition, the ratios between the isobar collisions of the mean transverse momenta [155] and net charge multiplicities [156] have been demonstrated to be reliable probes for determining the neutron skin difference between isobar nuclei. Consequently, these investigations indicate the possibility of utilizing observables in high-energy heavy-ion collisions to probe the neutron skin thickness and impose stringent constraints on the nuclear symmetry energy.

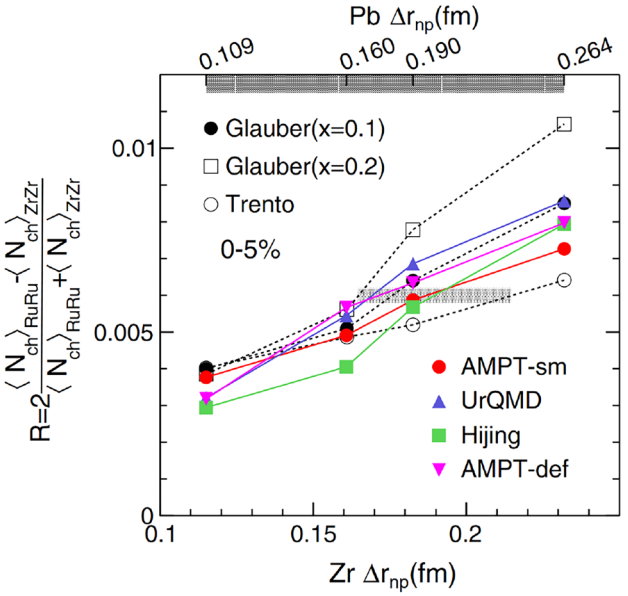

Fig. 13 (Color online) Correlation between the relative $\langle N_{ch}\rangle$ ratio (R) and the neutron skin thickness of Zr [152]

Recently, an attempt was made to determine the neutron skin of ^{208}Pb from ultra-relativistic nuclear collisions. As a typical heavy nucleus, ^{208}Pb has been the target of many dedicated efforts owing to its well-established nuclear structure. Ref. [157] analyzed the measurement results of particle distributions and their collective flow in ^{208}Pb+^{208}Pb collisions at ultra-relativistic energies performed at the Large Hadron Collider to extract the neutron skin thickness. Figure 14 shows an ultra-relativistic heavy-ion collision in the laboratory frame (a), where collisions deposit the energy density in the area of overlap (transverse plane) that is perpendicular to the beam direction (b). The QGP fluid evolves within the hydrodynamic model of heavy-ion collisions, as shown in Fig. 14c, until the confinement crossover is reached, after which the cooled QGP fluid is converted into a gas with Quantum Chromodynamics (QCD) resonance states that can further rescatter or decay to stable particles. Using global analysis tools, they inferred a neutron skin thickness of $\Delta r_{np} = 0.217 \pm 0.058$ fm, consistent with nuclear theory predictions and competitive in accuracy with a recent determination from parity-violating asymmetries in polarized electron scattering. Thus, a new experimental method was proposed to systematically measure neutron distributions in the ground state of atomic nuclei.

In another study, the STAR Collaboration presented a method for the photoproduction of vector mesons in ultra-peripheral nucleus–nucleus collisions to infer the average gluon density in the colliding nuclei and, hence, the neutron skins [147, 158].

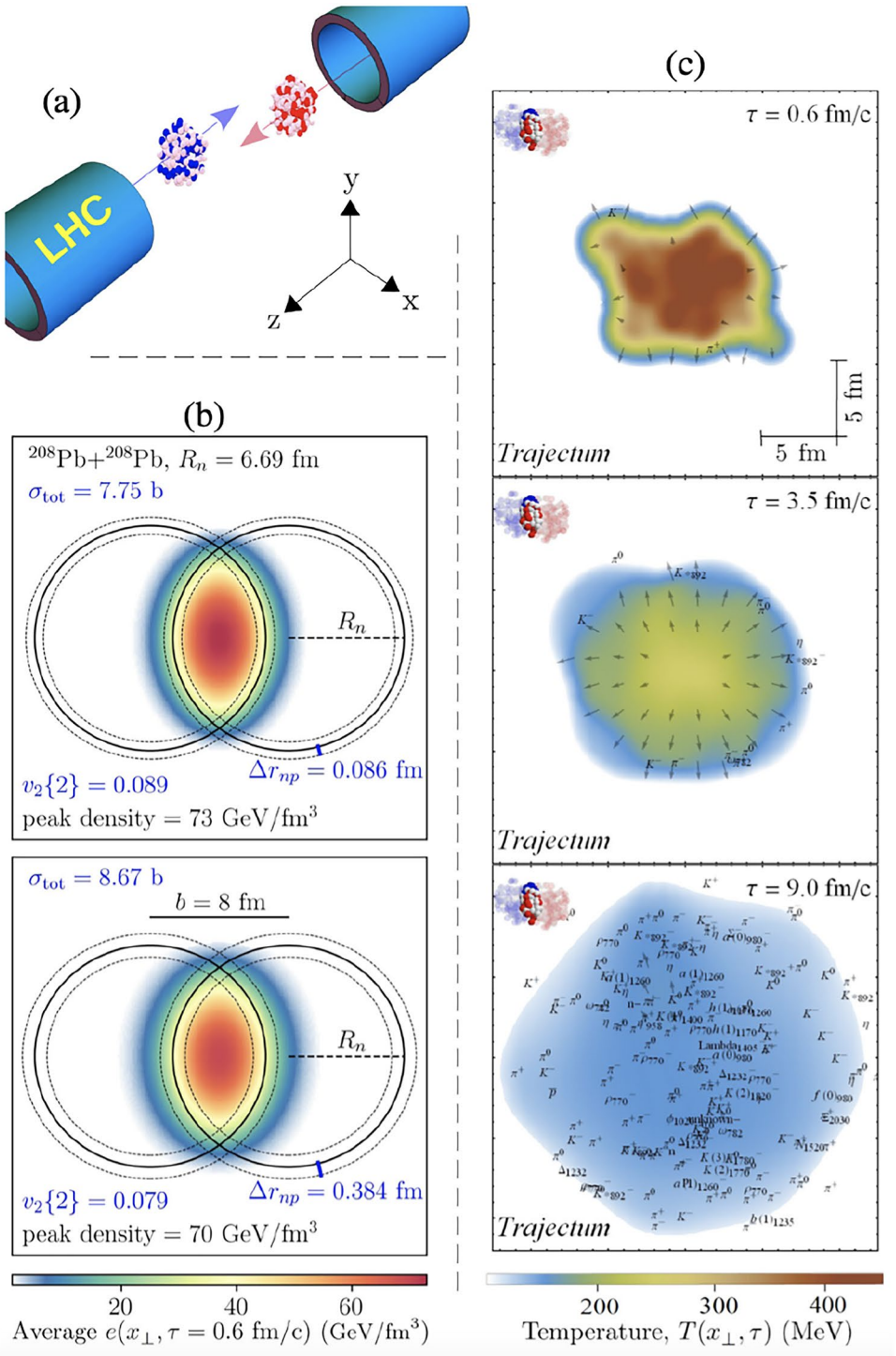

Fig. 14 (Color online) Neutron skin and collective flow in relativistic heavy-ion collisions. **a** Two ions collide with the impact parameter $b = 8$ fm. **b** The collision deposits energy in the interaction region depending on the extent of the neutron skin of ^{208}Pb nuclei. Here, $\Delta r_{\rm np} = 0.086$ fm (top) and $\Delta r_{\rm np} = 0.384$ fm (bottom) are used. **c** A single QGP evolves hydrodynamically and is converted into particles as it cools, while expanding both in z and in the transverse plane, and finally leads to azimuthal anisotropies, that is, collective flow [157]

When two relativistic heavy nuclei pass a distance of a few nuclear radii, the photon from one nucleus may interact through a virtual quark–antiquark pair with gluons from the other nucleus, forming a short-lived vector meson, such as ρ_0. In this experiment, polarization was used in diffractive photoproduction to observe a unique spin interference pattern in the angular distribution of $\rho_0 \to \pi^+\pi^-$ decay. The observed interference can be explained by the overlap of the two wave functions at a distance that is an order of magnitude larger than the ρ_0 travel distance within its lifetime. The strong interaction nuclear radii were extracted from these diffractive interactions and were found to be 6.53 ± 0.06 fm (^{197}Au) and 7.29 ± 0.08 fm (^{238}U), which are larger than the nuclear charge radii. The observable was demonstrated to be

sensitive to the nuclear geometry and quantum interference of nonidentical particles [158].

The progress in this direction using relativistic heavy-ion collisions is promising. Traditionally, neutron skin effects such as nuclear structure effects are believed to play an important role in low-energy nuclear physics. Because of the ultra-fast process of high-energy interactions, transient images of atomic nuclei can be photographed. An impressive study demonstrated that it is possible to obtain the deformation parameters of atomic nuclei, which are traditionally deduced from low-energy nuclear physics experiments, from the momentum distribution of particles produced in high-energy nuclear collisions [159]. Therefore, a bridge between high- and low-energy heavy-ion physics is established.

4 Experimental methods for the neutron halo and neutron skin

The emergence of new phenomena and physics in unstable nuclei far from the stability line poses a challenge to the traditional nuclear theory. To obtain explicit knowledge, it is necessary to generate and separate high-quality and high-intensity radioactive nuclear beams using accelerator facilities, which is the basis of experimental studies with the RNB. In this section, the experimental methods used for producing the RNB and probing the structure of the neutron halo and neutron skin are presented.

4.1 Production methods for the radioactive nuclear beam

Unstable nuclei in experimental studies are principally produced by RNB facilities. Various types of RNB facilities have been constructed and put into operation in major national laboratories of nuclear physics worldwide, including LISE at GANIL (France), A1200 at NCSL (United States), RIKEN projectile fragment separator (RIPS) at RIKEN (Japan), FRS at GSI (Germany), and RIBLL at HIRFL (China)[2]. In particular, the High Intensity heavy-ion Accelerator Facility (HIAF) is under construction at the Institute of Modern Physics, Chinese Academy of Sciences, and can generate high-intensity heavy-ion beams. The HIAF is believed to offer pioneering conditions for identifying new nuclides, expanding the nuclear landscape, and studying exotic phenomena and physics in nuclei far away from the stability line. Thus far, there are two basic approaches for generating RNBs: projectile fragmentation and isotope separation online (ISOL). The schematic of the two approaches is shown in Fig. 15 [160].

In the projectile fragmentation method, the primary accelerator directs a heavy-ion beam with a certain energy toward a thin production target, which produces a variety

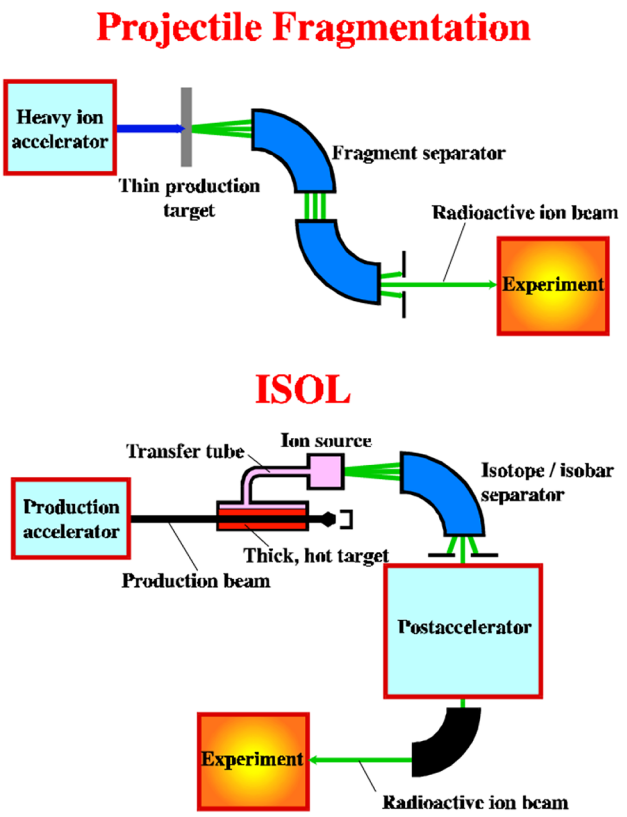

Fig. 15 (Color online) Schematic view for the two types of RNB facilities. [160]

of nuclear fragments with different charges and mass numbers. Subsequently, these fragments are selected by the electromagnetic separator based on the conditions of mass, charge, or momentum to obtain the secondary radioactive ion beam. This method enables the production of unstable nuclei with extremely short lifetimes in the μs range, including many secondary beams close to the neutron and proton drip lines. The maximum energies of the secondary beams are similar to those of the projectiles. Energy consumption can be reduced using an energy degrader when less energy is required in the experiment. Most second-generation RNB devices currently in use are projectile fragmentation–types owing to the lower technical difficulty, lower investment, and higher efficiency; for example, LISE, A1200, RIPS, FRS, and RIBLL. In the ISOL method, radioactive nuclei are produced through multifarious nuclear reactions by bombarding a thick target with high-intensity light particle beams with intermediate to high energies. Most, or even all, of the energy of the beam is lost at the target. The produced nuclei are ionized online and then selected by an isotope/isobar separator into the nuclear species of interest with low energy. The beam is eventually injected into a post-accelerator to be accelerated to an energy appropriate for the experimental terminal, which can be around and above the Coulomb

barrier (10-20 MeV/nucleon). This method is conducive to generating secondary radioactive beams with high intensity up to $10^{11} - 10^{12}$ pps (particles per second) and high quality while having a lifetime longer than 500ms because ISOL requires a certain amount of time to generate RNBs, making it difficult to obtain short-lived nuclei. Representative ISOL-type facilities include the ISOLDE at CERN, SPIRAL in GANIL, and TRIUMF in Canada. These two technologies have their own advantages and are technically complementary; therefore, they can be selected according to specific needs. More details regarding the RNB facilities and methods can be found in Refs. [2, 160, 161].

4.2 Experimental methods for the neutron halo

Since the discovery of the neutron–halo structure in ^{11}Li by Tanihata [162, 163], a series of observables sensitive to halo structures have been proposed and corresponding experimental methods have been developed. Compared with stable nuclei, halo nuclei exhibit many different properties. The two significant characteristics are the larger matter radii and the narrower width of the momentum distribution of valence nucleons. The direct measurement of nuclear reactions is the primary experimental method used for studying halo structures. However, this method is only suitable for nuclear ground states or long-lived excited states because the measurement is performed by bombarding a radioactive beam on the targets. The cross section of reactions and momentum distribution of fragments are two classical quantities that can be easily extracted in the direct measurement of nuclear reactions and are sensitive to exotic nuclear structures, especially halo structures. Most current experiments on halo nuclei have been performed by measuring these two quantities.

4.2.1 Reaction cross section

Experimentally, the charge radii of long-lived nuclei can be measured by electron scattering, proton scattering, and isotope shifts. However, the radii of nuclear matter are commonly determined by measuring the total cross section of nuclear reactions. The total nuclear reaction cross section is the sum of the probabilities of various reactions in nuclei–nuclei collisions, which depends on several factors such as the radius of the projectile and target nucleus and the collision energy. At high energies, the total nuclear reaction cross section (σ_R) is directly proportional to the square of the sum of the radii of the projectile (R_P) and the target (R_T) and can be expressed as follows:

$$\sigma_R = \pi(R_P + R_T)^2. \tag{8}$$

Of note, R_T is regarded as a known quantity because the target is a stable nucleus. Therefore, if σ_R is measured experimentally, and R_P or the density distribution of the projectile can be deduced using Eq. 8, which is the principle for measuring the radius of the nuclear matter.

Nevertheless, in reality, σ_R is dependent on energy, which can be well described by different theoretical models. In theory, the commonly used methods for calculating σ_R include the Kox parameterized formula [164], Shen parameterized formula [165], Glauber model based on semiclassical approximation of quantum mechanics [166], and microscopic transport theory such as Boltzmann–Uehling–Uhlenbeck [167, 168]. The density distribution of nuclear matter is an indispensable input in both Glauber and transport models. Therefore, by using these models to fit the experimental data of σ_R, the density distribution of nuclear matter can be extracted and the RMS radius of the nuclear matter can then be obtained. These methods for calculating σ_R have been widely used to study the effects of halos or skin structures and explore the reasons for their formation and characteristics.

In the experiments, σ_R is typically measured using a transmission method [169, 170]. When the beam passes through the target, the number of incident particles (N_0) correlates with the number of outgoing particles without a reaction (N_1), target thickness (t), and σ_R, which can be described as

$$N_1 = N_0 \exp(-\sigma_R t). \tag{9}$$

This expression can be transformed into

$$\sigma_R = -\ln(N_1/N_0)/t, \tag{10}$$

Hence, under the condition of a known t, σ_R can be deduced by measuring N_0 and N_1 in the experiments, which can be realized by placing the detectors in front of and behind the reaction target. However, this is an ideal scenario. In practice, neither the detection efficiency of the particles nor the transfer efficiency of the beam in devices can reach 100%. Moreover, the incident beam may react with all detectors in addition to the target. Consequently, these effects must be corrected by adding an empty target measurement, as described in Ref [169].

4.2.2 Fragment momentum distribution

Another quantity that can be directly measured in nuclear reactions is the momentum distribution of fragments through nucleon removal or breakup reactions, which can be either the core or valence nucleon(s). Nuclei with halo or exotic structures are generally considered to comprise a core and valence nucleons. The uncertainty principle qualitatively explains why the momentum distribution of fragments is sensitive to the halo structure. The narrower the momentum

distribution width, the smaller the intrinsic momentum fluctuation between the core and valence nucleons in the projectile rest system. According to the uncertainty principle, the core and valence nucleons form a relatively loose structure in coordinate space; that is, the spatial distribution of the valence nucleons diffuses away from the core, which is an essential characteristic of a halo structure. In addition, from the perspective of representation transformation in quantum mechanics, the wave functions in coordinate and momentum representations are closely related to each other through the Fourier transform. A nucleon with a wider density distribution in the coordinate space appears as a narrower distribution in the momentum space. Moreover, relative to the value of the wave function in momentum space at zero momentum, the full width at half maximum (FWHM) of momentum distribution is more sensitive to the halo structure.

In the projectile rest frame, the core part of the nucleus has exactly the same momentum as the valence nucleons but in the opposite direction. Therefore, the momentum distribution of the core can be measured to obtain the momentum distribution of valence nucleons in the experiments. In particular, for some neutron-rich nuclei, the valence nucleons are difficult to measure. Therefore, it is advisable to measure the momentum distribution of the core after the removal of valence nucleons. Instead of the transverse momentum, the measurement of the longitudinal momentum has fewer broadening effects introduced by the Coulomb deflection and multiple scattering in thick breakup targets, and its FWHM can effectively reflect the internal structure of the projectile nucleus [171].

Some measuring methods have been developed to extract the momentum distribution of fragments during the bombardment of projectiles on targets. Among them, the classical approaches include magnetic spectrometers, energy-loss spectrometers, and direct time-of-flight (TOF). A summary of the magnetic spectrometry and energy-loss spectrometry methods can be found in Ref. [172]. TOF analysis has shown that the velocity and momentum of a particle are determined by the time of a known flight distance [169, 173]. Compared with the measurements obtained using magnetic or energy-loss spectrometers, the direct TOF technique has the following advantages: First, it has a wider longitudinal momentum acceptance and a broader range of momentum spectra, which weakens the influence of distortion or dissociation on the spectrum width during the process of fitting. However, the momentum distribution data are still far away from the peak position. Second, the direct TOF method allows for the simultaneous measurement of the momentum distributions of different nuclear species produced by the same projectile, as well as the momentum distributions of fragments produced by different radioactive secondary beams. Consequently, it enables multiple groups of data to be obtained simultaneously in a single experiment and realizes simultaneous measurements of the total cross section of nuclear reactions and momentum distributions of fragments. It can also perform systematic research on different reaction systems in one experiment, which is of great significance for improving experimental efficiency.

4.2.3 Experiments at RIPS

In the experiments performed at RIPS in the RIKEN Ring Cyclotron Facility, the longitudinal momentum distribution of fragments is measured using a direct TOF technique, and the total reaction cross section is determined by a transmission method to investigate the exotic structure of the neutron-rich nucleus ^{15}C [169] and the proton-rich nucleus ^{23}Al [170]. The experimental setup for ^{15}C is illustrated in Fig. 16.

In the F0 chamber, the 110 MeV/nucleon ^{22}Ne primary beam was bombarded on a Be target to produce secondary beams of ^{14,15}C through projectile fragmentation reactions. In the dispersive focus plane F1, an Al wedge-shaped degrader was installed to separate the particles using the energy loss method. A delay-line readout parallel-plate avalanche counter (PPAC) was used to measure the beam position. The secondary beam was then directed onto achromatic focus F2. Two charge-division readout PPACs were used to determine the beam position and angle. Two Si detectors were used to measure the energy losses (ΔE), and an ultra-fast plastic scintillator was placed before the C reaction target to measure the TOF of PPAC at F1. Particle identification before the reaction target was performed using the $B\rho$–ΔE–TOF method. Subsequently, a quadrupole triplet was used to transport and focus the beam onto F3. Two delay-line readout PPACs were used to monitor the beam size and emittance angle. Another plastic scintillator provided a stop signal of the TOF from F2 to F3. Three Si detectors were used to measure the energy loss (ΔE), and an NaI(Tl) detector was used to measure the total energy (E). The particles were identified using the TOF–ΔE–E method. The longitudinal momentum distributions of the fragments after the removal of nucleons were determined from the TOF between the two plastic scintillators at F2 and F3. The positional information from the PPAC at F1 was used to derive the incident momentum of the beam. In addition, the reaction cross section was extracted with and without a reaction target using a transmission-type method via Eq. 10. The experimental data were reproduced by calculations using the few-body Glauber model to extract useful information on the density distribution of nuclear matter, nuclear radius, orbit, and the density distribution of valence nucleons for exotic nuclei far away from the stability line.

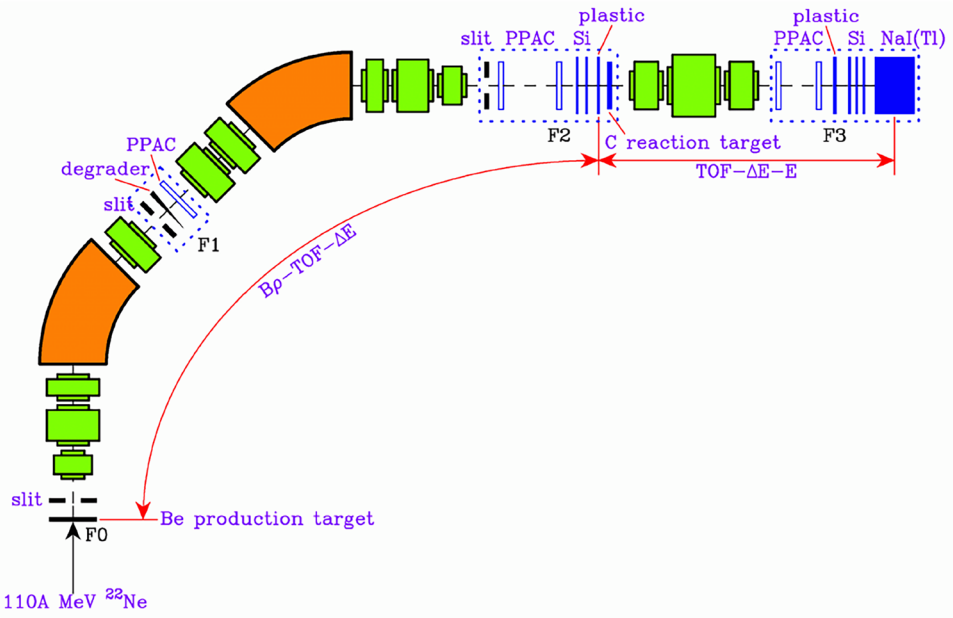

Fig. 16 (Color online) Experimental setup at the RIPS fragment separator. [169]

4.3 Experimental methods for neutron skin

The total nuclear matter radius can be determined from the total nuclear reaction cross section. To obtain the neutron skin thickness, it is necessary to know the RMS radii of protons and neutrons. Among the different cross sections in nuclear reactions, the charge-changing cross section is directly related to the proton radius. Therefore, the simultaneous determination of matter radii from the total nuclear reaction cross section and the proton radii from the charge-changing cross section in experiments provides a way to obtain the neutron skin thickness. In addition, all the observables discussed above, which exhibit a strong dependence on the neutron skin thickness, can be used as possible probes to determine the neutron skin thickness from experimental measurements. Measuring different observations requires different experimental devices and setups. For example, the identification of the projectile and its isotopes is vital for measuring neutron removal cross sections. The yield ratio of light particles was obtained by measuring the neutrons, protons, and charged particles. The measurement of the photon yield ratio requires the detection of γ rays. More importantly, if these observables are utilized in practice, more systematic studies are required to clarify the sensitivity of each observable parameter to the neutron skin thickness. Only if the accuracy of the extracted neutron skin thickness satisfies the expectations will the observable be an ideal experimental probe. For example, if the uncertainty in the neutron-to-proton yield ratio reaches 5%, the estimated error in the neutron skin thickness can be approximately 0.1fm [76]. In addition to intermediate-energy heavy-ion collisions, some probes are expected to be proposed to detect the neutron skin thickness in high-energy reactions, which is limited to the ability to study the neutron skin of some stable nuclei in current studies. If collisions of unstable nuclei at high energies can be performed in future, some sensitive probes in high-energy nuclear collisions could also be used to study the structure of the neutron skin.

In addition to the above methods, the measurement of parity-violating asymmetry in the elastic scattering of polarized electrons performed at the Thomas Jefferson National Accelerator Facility has received considerable attention. This experiment provides a more precise electroweak determination of the neutron skin thickness. The neutron skin thicknesses of ^{208}Pb ($\Delta r_{\rm np}^{208}$) and ^{48}Ca ($\Delta r_{\rm np}^{48}$) were measured. The first measurement for ^{208}Pb (PREX-1) inferred $\Delta r_{\rm np}^{208}$ (PREX1) $= 0.33^{+0.16}_{-0.18}$ fm [114], and a new result (PREX-2) with greatly improved precision was then reported $\Delta r_{\rm np}^{208}$ (PREX2) $= 0.283 \pm 0.071$ fm [174]. In addition, the latest measurements for ^{48}Ca (CREX) concluded that $\Delta r_{\rm np}^{48}$(CREX) was 0.121 ± 0.026(exp) ± 0.024(model) fm [175]. Within a specific class of relativistic EDFs, the value of $L = 106 \pm 37$ MeV was constrained by $\Delta r_{\rm np}^{208}$(PREX2) [176], which indicates a stiff EOS that is fairly larger than previous theoretical and experimental results. A re-analysis of the PREX data using different families of nuclear EDFs suggests $L = 54 \pm 8$ MeV, implying a relatively soft EOS. Thus, the predicted value of the L parameter based on the same PREX-2 experiment is still under discussion. Very recently, by using 207 non-relativistic and relativistic mean-field models, the values of L were deduced in the range of $76 - 165$ MeV from $\Delta r_{\rm np}^{208}$(PREX2) and $0 - 51$ MeV from $\Delta r_{\rm np}^{48}$(CREX), which indicates that there is no overlap

between the two ranges of L, making it a major problem to be solved [177]. With the Bayesian inference method and the Skyrme EDF, the combined analysis of CREX and PREX-2 data results in a softer symmetry energy and thinner neutron skin thickness, that is, $L = 17.1^{+39.3}_{-36.0}$ MeV, $\Delta r_{\rm np}^{208} = 0.136^{+0.059}_{-0.056}$ fm, and $\Delta r_{\rm np}^{48} = 0.150^{+0.031}_{-0.030}$ fm at a 90% confidence level [178]. These inconsistent results call for further theoretical and experimental investigations.

5 Discussion and Summary

The structure of the neutron skin is an interesting phenomenon for neutron-rich nuclei far away from the stability line. Compared with the stable nuclei, which have similar density distributions of neutrons and protons, the size of the neutron skin is closely related to the single-particle orbit and isospin evolution of the shell structure. The systematic study of the neutron skin is of great importance for a deep understanding of the essence of nuclear forces. In addition, the structure of the neutron skin is closely related to the properties of the EOS of asymmetric nuclear matter and neutron stars. Owing to the low experimental accuracy of the neutron radius, the exploration of effective experimental observables that are sensitive to the neutron skin thickness has become a hot topic in nuclear physics.

Because the total reaction cross section $\sigma_{\rm R}$ is one of the most important observables for determining the size of nuclei, Shen et al. systematically studied $\sigma_{\rm R}$ for heavy-ion collisions and its relation with isospin [165]. By analyzing the variation in $\sigma_{\rm R}$ with energy from low (< 10 MeV/nucleon) to intermediate energies for a wide variety of projectile-target combinations, a unified parameterized formula for $\sigma_{\rm R}$ was proposed that can reproduce data from low to intermediate energies. The effects of the neutron skin, ground-state deformation, and surface diffuseness of the neutron distribution on $\sigma_{\rm R}$ were studied via a modified microscopic model in which the difference between neutron and proton distributions in the nucleus was considered. Assuming that the surface diffuseness of the neutron distribution increases linearly with $(N - Z)$, the modified microscopic model can reproduce the dependence of $\sigma_{\rm R}$ on the neutron excess well. The possibility of extracting the neutron skin thickness through a neutron-rich flow in a damped collision for neutron-rich reaction systems was also discussed. These results are important for further studies on nuclear size and neutron skin thickness.

In recent years, based on various theoretical models, some quantities of nucleus–nucleus collisions or nuclear structures have been demonstrated to have strong correlations with the neutron skin thickness, making it possible to extract information on the neutron skin and further constrain the properties of the EOS and neutron stars. In particular, relativistic heavy-ion collisions provide a new avenue for investigating nuclear structures, such as the neutron skin, deformation, and clustering structures. Studies of the structures and collisions of atomic nuclei have become increasingly intersectional and integrated. Further studies are essential not only for the precise experimental determination of the proposed observables but also for the search for cleaner probes for neutron skin with higher sensitivity.

References

1. X.W. Xia, Y. Lim, P.W. Zhao et al., The limits of the nuclear landscape explored by the relativistic continuum Hartree–Bogoliubov theory. At. Data Nucl. Data Tables **121–122**, 1–215 (2018). https://doi.org/10.1016/j.adt.2017.09.001
2. C.W. Ma, H.L. Wei, X.Q. Liu et al., Nuclear fragments in projectile fragmentation reactions. Pro. Part. Nucl. Phys. **121**, 103911 (2021). https://doi.org/10.1016/j.ppnp.2021.103911
3. F. Kondev, M. Wang, W.J. Huang et al., The Nubase 2020 evaluation of nuclear physics properties. Chin. Phys. C **45**, 030001 (2021). https://doi.org/10.1088/1674-1137/abddae
4. Y.F. Luo, X.L. Yan, M. Wang et al., Review and a new design of the chart of nuclides. Nucl. Phys. Rev. **40**, 121–139 (2023). https://doi.org/10.11804/NuclPhysRev.40.2023018
5. I. Tanihata, H. Savajols, R. Kanungo, Recent experimental progress in nuclear halo structure studies. Prog. Part. Nucl. Phys. **68**, 215–313 (2013). https://doi.org/10.1016/j.ppnp.2012.07.001
6. A. Bracco, The NuPECC long range plan 2017: perspectives in nuclear physics. Nucl. Phys. News **27**, 3–4 (2017). https://doi.org/10.1080/10619127.2017.1352311
7. B. Blank, M. Borge, Nuclear structure at the proton drip line: advances with nuclear decay studies. Pro. Part. Nucl. Phys. **60**, 403–483 (2008). https://doi.org/10.1016/j.ppnp.2007.12.001
8. L. Zhou, S.M. Wang, D.Q. Fang et al., Recent progress in two-proton radioactivity. Nucl. Sci. Tech. **33**, 105 (2022). https://doi.org/10.1007/s41365-022-01091-1
9. E.B. Huo, T.T. Sun, K.R. Li et al., Continuum Skyrme Hartree–Fock–Bogoliubov theory with Green's function method for neutron-rich Ca, Ni, Zr, Sn isotopes. Nucl. Sci. Tech. **34**, 105 (2022). https://doi.org/10.1007/s41365-023-01261-9
10. D.Q. Fang, Neutron skin thickness and its effects in nuclear reactions. Nucl. Tech. (in Chinese) **46**, 080016 (2023). https://doi.org/10.11889/j.0253-3219.2023.hjs.46.080016
11. I. Angeli, A consistent set of nuclear rms charge radii: properties of the radius surface $R(N, Z)$. At. Data Nucl. Data Tables **87**, 185–206 (2004). https://doi.org/10.1016/j.adt.2004.04.002

12. G. Hoffmann, L. Ray, M. Barlett et al., Elastic scattering of 500 MeV polarized protons from ^{40,48}Ca, ^{90}Zr, and ^{208}Pb, and breakdown of the impulse approximation at small momentum transfer. Phys. Rev. Lett. **47**, 1436–1440 (1981). https://doi.org/10.1103/PhysRevLett.47.1436
13. V. Starodubsky, N. Hintz, Extraction of neutron densities from elastic proton scattering by ^{206,207,208}Pb at 650 MeV. Phys. Rev. C **49**, 2118–2135 (1994). https://doi.org/10.1103/PhysRevC.49.2118
14. A. Krasznahorkay, J. Bacelar, J. Bordewijk et al., Excitation of the isovector giant dipole resonance by inelastic α scattering and the neutron skin of nuclei. Phys. Rev. Lett. **66**, 1287–1290 (1991). https://doi.org/10.1103/PhysRevLett.66.1287
15. G. Satchler, Isospin and macroscopic models for the excitation of giant resonances and other collective states. Nucl. Phys. A **472**, 215–236 (1987). https://doi.org/10.1016/0375-9474(87)90208-9
16. A. Krasznahorkay, M. Fujiwara, P. van Aarle et al., Excitation of isovector spin-dipole resonances and neutron skin of nuclei. Phys. Rev. Lett. **82**, 3216–3219 (1999). https://doi.org/10.1103/PhysRevLett.82.3216
17. P. Lubiński, J. Jastrzębski, A. Trzcińska et al., Composition of the nuclear periphery from antiproton absorption. Phys. Rev. C **57**, 2962–2973 (1998). https://doi.org/10.1103/PhysRevC.57.2962
18. A. Trzcińska, J. Jastrzębski, P. Lubiński et al., Neutron density distributions deduced from antiprotonic atoms. Phys. Rev. Lett. **87**, 082501 (2001). https://doi.org/10.1103/PhysRevLett.87.082501
19. L. Ray, G. Hoffmann, W. Coker, Nonrelativistic and relativistic descriptions of proton-nucleus scattering. Phys. Rep. **212**, 223–328 (1992). https://doi.org/10.1016/0370-1573(92)90156-T
20. J. Lattimer, M. Prakash, Neutron star observations: prognosis for equation of state constraints. Phys. Rep. **442**, 109–165 (2007). https://doi.org/10.1016/j.physrep.2007.02.003
21. M. Baldo, C. Maieron, P. Schuck et al., Low densities in nuclear and neutron matters and in the nuclear surface. Nucl. Phys. A **736**, 241–254 (2004). https://doi.org/10.1016/j.nuclphysa.2004.03.148
22. X. Roca-Maza, N. Paar, Nuclear equation of state from ground and collective excited state properties of nuclei. Prog. Part. Nucl. Phys. **101**, 96–176 (2018). https://doi.org/10.1016/j.ppnp.2018.04.001
23. W.Z. Jiang, R.Y. Yang, S.N. Wei, Strangeness to increase the density of finite nuclear systems in constraining the high-density nuclear equation of state. Nucl. Sci. Tech. **28**, 180 (2017). https://doi.org/10.1007/s41365-017-0333-5
24. H. Yu, D.Q. Fang, Y.G. Ma, Investigation of the symmetry energy of nuclear matter using isospin-dependent quantum molecular dynamics. Nucl. Sci. Tech. **31**, 61 (2020). https://doi.org/10.1007/s41365-020-00766-x
25. N.B. Zhang, B.A. Li, Astrophysical constraints on a parametric equation of state for neutron-rich nucleonic matter. Nucl. Sci. Tech. **29**, 178 (2018). https://doi.org/10.1007/s41365-018-0515-9
26. G.F. Wei, X. Huang, Q. Zhi et al., Effects of the momentum dependence of nuclear symmetry potential on pion observables in Sn+Sn collisions at 270 MeV/nucleon. Nucl. Sci. Tech. **33**, 163 (2022). https://doi.org/10.1007/s41365-022-01146-3
27. B.A. Li, Nuclear symmetry energy extracted from laboratory experiments. Nucl. Phys. News **27**, 7–11 (2017). https://doi.org/10.1080/10619127.2017.1388681
28. L. Li, F.Y. Wang, Y.X. Zhang, Isospin effects on intermediate mass fragments at intermediate energy-heavy ion collisions. Nucl. Sci. Tech. **33**, 58 (2022). https://doi.org/10.1007/s41365-022-01050-w
29. J. Liu, C. Gao, N. Wan et al., Basic quantities of the equation of state in isospin asymmetric nuclear matter. Nucl. Sci. Tech. **32**, 117 (2021). https://doi.org/10.1007/s41365-021-00955-2
30. L.W. Chen, Symmetry energy systematics and its high density behavior. EPJ Web Conf. **88**, 00017 (2015). https://doi.org/10.1051/epjconf/20158800017
31. L.W. Chen, C.M. Ko, B.A. Li, Nuclear matter symmetry energy and the neutron skin thickness of heavy nuclei. Phys. Rev. C **72**, 064309 (2005). https://doi.org/10.1103/PhysRevC.72.064309
32. B. Brown, Neutron radii in nuclei and the neutron equation of state. Phys. Rev. Lett. **85**, 5296–5299 (2000). https://doi.org/10.1103/PhysRevLett.85.5296
33. S. Typel, B. Brown, Neutron radii and the neutron equation of state in relativistic models. Phys. Rev. C **64**, 027302 (2001). https://doi.org/10.1103/PhysRevC.64.027302
34. R. Furnstahl, Neutron radii in mean-field models. Nucl. Phys. A **706**, 85–110 (2002). https://doi.org/10.1016/S0375-9474(02)00867-9
35. S. Karataglidis, K. Amos, B. Brown et al., Discerning the neutron density distribution of ^{208}Pb from nucleon elastic scattering. Phys. Rev. C **65**, 044306 (2002). https://doi.org/10.1103/PhysRevC.65.044306
36. M. Centelles, X. Roca-Maza, X. Viñas et al., Nuclear symmetry energy probed by neutron skin thickness of nuclei. Phys. Rev. Lett. **102**, 122502 (2009). https://doi.org/10.1103/PhysRevLett.102.122502
37. W.B. He, Q.F. Li, Y.G. Ma et al., Machine learning in nuclear physics at low and intermediate energies. Sci. China Phys. Mech. Astron. **66**, 282001 (2023). https://doi.org/10.1007/s11433-023-2116-0
38. Z. Zhang, L.W. Chen, Constraining the symmetry energy at subsaturation densities using isotope binding energy difference and neutron skin thickness. Phys. Lett. B **726**, 234–238 (2013). https://doi.org/10.1016/j.physletb.2013.08.002
39. J.M. Lattimer, M. Prakash, The physics of neutron stars. Science **304**, 536–542 (2004). https://doi.org/10.1126/science.1090720
40. B. Abbott, R. Abbott, T. Abbott et al., Gw170817: observation of gravitational waves from a binary neutron star inspiral. Phys. Rev. Lett. **119**, 161101 (2017). https://doi.org/10.1103/PhysRevLett.119.161101
41. F. Özel, G. Baym, T. Güver, Astrophysical measurement of the equation of state of neutron star matter. Phys. Rev. D **82**, 101301 (2010). https://doi.org/10.1103/PhysRevD.82.101301
42. A. Steiner, J. Lattimer, E. Brown, The equation of state from observed masses and radii of neutron stars. Astrophys. J. **722**, 33 (2010). https://doi.org/10.1088/0004-637X/722/1/33
43. J. Carriere, C. Horowitz, J. Piekarewicz, Low-mass neutron stars and the equation of state of dense matter. Astrophys. J. **593**, 463 (2003). https://doi.org/10.1086/376515
44. C. Horowitz, J. Piekarewicz, Neutron star structure and the neutron radius of ^{208}Pb. Phys. Rev. Lett. **86**, 5647–5650 (2001). https://doi.org/10.1103/PhysRevLett.86.5647
45. B. Link, R. Epstein, J. Lattimer, Pulsar constraints on neutron star structure and equation of state. Phys. Rev. Lett. **83**, 3362–3365 (1999). https://doi.org/10.1103/PhysRevLett.83.3362
46. J. Lattimer, M. Prakash, Neutron star structure and the equation of state. Astrophys. J. **550**, 426 (2001). https://doi.org/10.1086/319702
47. W.J. Xie, Z.W. Ma, J.H. Guo, Bayesian inference of the crust-core transition density via the neutron-star radius and neutron-skin thickness data. Nucl. Sci. Tech. **34**, 91 (2023). https://doi.org/10.1007/s41365-023-01239-7
48. D. Page, J. Lattimer, M. Prakash et al., Minimal cooling of neutron stars: a new paradigm. Astrophys. J. Suppl. **155**, 623 (2004). https://doi.org/10.1086/424844

49. C. Horowitz, J. Piekarewicz, Constraining urca cooling of neutron stars from the neutron radius of ^{208}Pb. Phys. Rev. C **66**, 055803 (2002). https://doi.org/10.1103/PhysRevC.66.055803
50. F. Fattoyev, J. Piekarewicz, Sensitivity of the moment of inertia of neutron stars to the equation of state of neutron-rich matter. Phys. Rev. C **82**, 025810 (2010). https://doi.org/10.1103/PhysRevC.82.025810
51. A. Steiner, M. Prakash, J. Lattimer et al., Isospin asymmetry in nuclei and neutron stars. Phys. Rep. **411**, 325–375 (2005). https://doi.org/10.1016/j.physrep.2005.02.004
52. B.A. Li, M. Magno, Curvature-slope correlation of nuclear symmetry energy and its imprints on the crust-core transition, radius, and tidal deformability of canonical neutron stars. Phys. Rev. C **102**, 045807 (2020). https://doi.org/10.1103/PhysRevC.102.045807
53. J. Lattimer, M. Prakash, The equation of state of hot, dense matter and neutron stars. Phys. Rep. **621**, 127–164 (2016). https://doi.org/10.1016/j.physrep.2015.12.005
54. F. Fattoyev, J. Piekarewicz, C. Horowitz, Neutron skins and neutron stars in the multimessenger era. Phys. Rev. Lett. **120**, 172702 (2018). https://doi.org/10.1103/PhysRevLett.120.172702
55. Y.X. Zhang, M. Liu, C.J. Xia et al., Constraints on the symmetry energy and its associated parameters from nuclei to neutron stars. Phys. Rev. C **101**, 034303 (2020). https://doi.org/10.1103/PhysRevC.101.034303
56. F. Fattoyev, J. Piekarewicz, Neutron skins and neutron stars. Phys. Rev. C **86**, 015802 (2012). https://doi.org/10.1103/PhysRevC.86.015802
57. W. Newton, R. Preston, L. Balliet et al., From neutron skins and neutron matter to the neutron star crust. Phys. Lett. B **834**, 137481 (2022). https://doi.org/10.1016/j.physletb.2022.137481
58. T. Brohm, K. Schmidt, Statistical abrasion of nucleons from realistic nuclear-matter distributions. Nucl. Phys. A **569**, 821–832 (1994). https://doi.org/10.1016/0375-9474(94)90386-7
59. D.Q. Fang, Y.G. Ma, X.Z. Cai et al., Neutron removal cross section as a measure of neutron skin. Phys. Rev. C **81**, 047603 (2010). https://doi.org/10.1103/PhysRevC.81.047603
60. D.Q. Fang, Y.G. Ma, X.Z. Cai et al., Effects of neutron skin thickness in peripheral nuclear reactions. Chin. Phys. Lett. **28**, 102102 (2011). https://doi.org/10.1088/0256-307X/28/10/102102
61. T. Aumann, C. Bertulani, F. Schindler et al., Peeling off neutron skins from neutron-rich nuclei: constraints on the symmetry energy from neutron-removal cross sections. Phys. Rev. Lett. **119**, 262501 (2017). https://doi.org/10.1103/PhysRevLett.119.262501
62. J. Aichelin, Quantum molecular dynamics-a dynamical microscopic n-body approach to investigate fragment formation and the nuclear equation of state in heavy ion collisions. Phys. Rep. **202**, 233–360 (1991). https://doi.org/10.1016/0370-1573(91)90094-3
63. Y.X. Zhang, N. Wang, Q.F. Li et al., Progress of quantum molecular dynamics model and its applications in heavy ion collisions. Front. Phys. **15**, 1–64 (2020). https://doi.org/10.1007/s11467-020-0961-9
64. H. Wolter, M. Colonna, D. Cozma et al., Transport model comparison studies of intermediate-energy heavy-ion collisions. Prog. Part. Nucl. Phys. **125**, 103962 (2022). https://doi.org/10.1016/j.ppnp.2022.103962
65. M. Colonna, Y.X. Zhang, Y.J. Wang et al., Comparison of heavy-ion transport simulations: mean-field dynamics in a box. Phys. Rev. C **104**, 024603 (2021). https://doi.org/10.1103/PhysRevC.104.024603
66. J. Aichelin, A. Bohnet, G. Peilert et al., Quantum molecular dynamics approach to heavy ion collisions: description of the model, comparison with fragmentation data, and the mechanism of fragment formation. Phys. Rev. C **37**, 2451–2468 (1988). https://doi.org/10.1103/PhysRevC.37.2451
67. Z.Q. Feng, Nuclear dynamics and particle production near threshold energies in heavy-ion collisions. Nucl. Sci. Tech. **29**, 40 (2018). https://doi.org/10.1007/s41365-018-0379-z
68. L.W. Chen, F.S. Zhang, G.M. Jin, Analysis of isospin dependence of nuclear collective flow in an isospin-dependent quantum molecular dynamics model. Phys. Rev. C **58**, 2283–2291 (1998). https://doi.org/10.1103/PhysRevC.58.2283
69. X.G. Cao, X.Z. Cai, Y.G. Ma et al., Nucleon-nucleon momentum-correlation function as a probe of the density distribution of valence neutrons in neutron-rich nuclei. Phys. Rev. C **86**, 044620 (2012). https://doi.org/10.1103/PhysRevC.86.044620
70. J.Y. Liu, W.J. Guo, Z.Z. Ren et al., Special roles of loose neutron-halo nucleus structure on the fragmentation and momentum dissipation in heavy ion collisions. Phys. Lett. B **617**, 24–32 (2005). https://doi.org/10.1016/j.physletb.2005.05.011
71. C. Tao, Y.G. Ma, G.Q. Zhang et al., Pygmy and giant dipole resonances by coulomb excitation using a quantum molecular dynamics model. Phys. Rev. C **87**, 014621 (2013). https://doi.org/10.1103/PhysRevC.87.014621
72. Y.G. Ma, W.Q. Shen, Onset of multifragmentation in intermediate energy light asymmetrical collisions. Phys. Rev. C **51**, 710–715 (1995). https://doi.org/10.1103/PhysRevC.51.710
73. F.S. Zhang, L.W. Chen, Z.Y. Ming et al., Isospin dependence of nuclear multifragmentation in ^{112}Sn+^{112}Sn and ^{124}Sn+^{124}Sn collisions at 40 MeV/nucleon. Phys. Rev. C **60**, 064604 (1999). https://doi.org/10.1103/PhysRevC.60.064604
74. Y.G. Ma, Y.B. Wei, W.Q. Shen et al., Surveying the nucleon-nucleon momentum correlation function in the framework of quantum molecular dynamics model. Phys. Rev. C **73**, 014604 (2006). https://doi.org/10.1103/PhysRevC.73.014604
75. Y.G. Ma, W.Q. Shen, Correlation functions and the disappearance of rotational collective motion in nucleus-nucleus collisions below 100 MeV/nucleon. Phys. Rev. C **51**, 3256–3263 (1995). https://doi.org/10.1103/PhysRevC.51.3256
76. X.Y. Sun, D.Q. Fang, Y.G. Ma et al., Neutron/proton ratio of nucleon emissions as a probe of neutron skin. Phys. Lett. B **682**, 396–400 (2010). https://doi.org/10.1016/j.physletb.2009.11.031
77. X.Y. Sun, D.Q. Fang, Y.G. Ma et al., A new probe of neutron skin thickness. Chin. Phys. C **35**, 6 (2011). https://doi.org/10.1088/1674-1137/35/6/009
78. M.Q. Ding, D.Q. Fang, Y.G. Ma, Effects of neutron-skin thickness on light-particle production. Phys. Rev. C **109**, 024616 (2024). https://doi.org/10.1103/PhysRevC.109.024616
79. Z.T. Dai, D.Q. Fang, Y.G. Ma et al., Triton/^{3}He ratio as an observable for neutron-skin thickness. Phys. Rev. C **89**, 014613 (2014). https://doi.org/10.1103/PhysRevC.89.014613
80. T.Z. Yan, S. Li, Yield ratios of light particles as a probe of the proton skin of a nucleus and its centrality dependence. Phys. Rev. C **101**, 054601 (2020). https://doi.org/10.1103/PhysRevC.101.054601
81. T.Z. Yan, S. Li, Impact parameter dependence of the yield ratios of light particles as a probe of neutron skin. Nucl. Sci. Tech. **30**, 43 (2019). https://doi.org/10.1007/s41365-019-0572-8
82. J. Su, W. Trautmann, L. Zhu et al., Dynamical properties and secondary decay effects of projectile fragmentations in ^{124}Sn, ^{107}Sn + ^{120}Sn collisions at 600 MeV/nucleon. Phys. Rev. C **98**, 014610 (2018). https://doi.org/10.1103/PhysRevC.98.014610
83. C.W. Ma, X.B. Wei, X.X. Chen et al., Precise machine learning models for fragment production in projectile fragmentation reactions using bayesian neural networks. Chin. Phys. C **46**, 074104 (2022). https://doi.org/10.1088/1674-1137/ac5efb
84. X.B. Wei, H.L. Wei, Y.T. Wang et al., Multiple-models predictions for drip line nuclides in projectile fragmentation of

^{40,48}Ca, ^{58,64}Ni, and ^{78,86}Kr at 140 MeV/u. Nucl. Sci. Tech. **33**, 155 (2022). https://doi.org/10.1007/s41365-022-01137-4
85. E. Friedlander, H. Heckman, *Treatise on heavy-ion science. Vol. 4: extreme nuclear states*, (Springer, New York, 1985) https://doi.org/10.1007/978-1-4615-8097-3
86. V. Baran, M. Colonna, V. Greco et al., Reaction dynamics with exotic nuclei. Phys. Rep. **410**, 335–466 (2005). https://doi.org/10.1016/j.physrep.2004.12.004
87. Z.T. Dai, D.Q. Fang, Y.G. Ma et al., Effect of neutron skin thickness on projectile fragmentation. Phys. Rev. C **91**, 034618 (2015). https://doi.org/10.1103/PhysRevC.91.034618
88. D. Peng, C.W. Ma, C.Y. Qiao et al., Isoscaling properties for neutron-rich fragments in highly asymmetric heavy ion collision systems. Chin. Phys. C **48**, 064103 (2024). https://doi.org/10.1088/1674-1137/ad33bd
89. C.W. Ma, Y.J. Duan, Y.F. Guo et al., A possible probe to neutron-skin thickness by fragment parallel momentum distribution in projectile fragmentation reactions. Nucl. Sci. Tech. **35**, 99 (2024). https://doi.org/10.1007/s41365-024-01455-9
90. J.P. Yang, X. Chen, Y. Cui et al., Probing the neutron skin of unstable nuclei with heavy-ion collisions. Universe **9**, 206 (2023). https://doi.org/10.3390/universe9050206
91. C. Bertulani, J. Valencia, Neutron skins as laboratory constraints on properties of neutron stars and on what we can learn from heavy ion fragmentation reactions. Phys. Rev. C **100**, 015802 (2019). https://doi.org/10.1103/PhysRevC.100.01580
92. H.L. Wei, X. Zhu, C. Yuan, Configurational information entropy analysis of fragment mass cross distributions to determine the neutron skin thickness of projectile nuclei. Nucl. Sci. Tech. **33**, 111 (2022). https://doi.org/10.1007/s41365-022-01096-w
93. C.W. Ma, Y.P. Liu, H.L. Wei et al., Determination of neutron-skin thickness using configurational information entropy. Nucl. Sci. Tech. **33**, 6 (2022). https://doi.org/10.1007/s41365-022-00997-0
94. Y.G. Ma, G.H. Liu, X.Z. Cai et al., Hard-photon flow and photon-photon correlation in intermediate-energy heavy-ion collisions. Phys. Rev. C **85**, 024618 (2012). https://doi.org/10.1103/PhysRevC.85.024618
95. X.G. Deng, Y.G. Ma, Magnetic field effects on photon emission in intermediate energy heavy-ion collisions. Eur. Phys. J. A **54**, 204 (2018). https://doi.org/10.1140/epja/i2018-12635-x
96. S.S. Wang, Y.G. Ma, D.Q. Fang et al., Effects of neutron-skin thickness on direct hard photon emission from reactions induced by the neutron-rich projectile ^{50}Ca. Phys. Rev. C **105**, 034616 (2022). https://doi.org/10.1103/PhysRevC.105.034616
97. G.F. Wei, Probing the neutron-skin thickness by photon production from reactions induced by intermediate-energy protons. Phys. Rev. C **92**, 014614 (2015). https://doi.org/10.1103/PhysRevC.92.014614
98. W.M. Guo, B.A. Li, G.C. Yong, Interplay of effects of neutron skins in coordinate space and proton skins in momentum space on emission of hard photons in heavy-ion collisions near the fermi energy. Phys. Rev. C **108**, 034617 (2023). https://doi.org/10.1103/PhysRevC.108.034617
99. L. Ou, Z.X. Li, X.Z. Wu et al., Disentangling the effects of thickness of the neutron skin and symmetry potential in nucleon induced reactions on sn isotopes. Chin. Phys. Lett. **26**, 052501 (2009). https://doi.org/10.1088/0256-307X/26/5/052501
100. L. Ou, Z.X. Li, X.Z. Wu, Dynamical isospin effects in nucleon-induced reactions. Phys. Rev. C **78**, 044609 (2008). https://doi.org/10.1103/PhysRevC.78.044609
101. C. Qi, R. Liotta, R. Wyss, Recent developments in radioactive charged-particle emissions and related phenomena. Pro. Part. Nucl. Phys. **105**, 214–251 (2019). https://doi.org/10.1016/j.ppnp.2018.11.003
102. G. Gamow, Zur quantentheorie des atomkernes. Z. Physik **51**, 204–212 (1928). https://doi.org/10.1007/BF01343196
103. S. Typel, G. Röpke, T. Klähn et al., Composition and thermodynamics of nuclear matter with light clusters. Phys. Rev. C **81**, 015803 (2010). https://doi.org/10.1103/PhysRevC.81.015803
104. D. Delion, R. Liotta, Shell-model representation to describe α emission. Phys. Rev. C **87**, 041302 (2013). https://doi.org/10.1103/PhysRevC.87.041302
105. K. Hagel, R. Wada, L. Qin et al., Experimental determination of in-medium cluster binding energies and mott points in nuclear matter. Phys. Rev. Lett. **108**, 062702 (2012). https://doi.org/10.1103/PhysRevLett.108.0627026
106. S. Typel, Neutron skin thickness of heavy nuclei with α-particle correlations and the slope of the nuclear symmetry energy. Phys. Rev. C **89**, 064321 (2014). https://doi.org/10.1103/PhysRevC.89.064321
107. M. Oertel, M. Hempel, T. Klähn et al., Equations of state for supernovae and compact stars. Rev. Mod. Phys. **89**, 015007 (2017). https://doi.org/10.1103/RevModPhys.89.015007
108. J. Tanaka, Z.H. Yang, S. Typel et al., Formation of α clusters in dilute neutron-rich matter. Science **371**, 260–264 (2021). https://doi.org/10.1126/science.abe4688
109. Q. Zhao, Y. Suzuki, J. He et al., α clustering and neutron-skin thickness of carbon isotopes. Eur. Phys. J. A **57**, 157 (2021). https://doi.org/10.1140/epja/s10050-021-00465-0
110. N. Wan, C. Xu, Z.Z. Ren, Exploring the sensitivity of α -decay half-life to neutron skin thickness for nuclei around ^{208} Pb. Nucl. Sci. Tech. **28**, 22 (2017). https://doi.org/10.1007/s41365-016-0174-7
111. W. Seif, N. Antonenko, G. Adamian et al., Correlation between observed α decays and changes in neutron or proton skins from parent to daughter nuclei. Phys. Rev. C **96**, 054328 (2017). https://doi.org/10.1103/PhysRevC.96.054328
112. C. Xu, Z. Ren, J. Liu, Attempt to link the neutron skin thickness of ^{208}Pb with the symmetry energy through cluster radioactivity. Phys. Rev. C **90**, 064310 (2014). https://doi.org/10.1103/PhysRevC.90.064310
113. D.D. Ni, Z.Z. Ren, Effects of differences between neutron and proton density distributions on α-decay half-lives. Phys. Rev. C **92**, 054322 (2015). https://doi.org/10.1103/PhysRevC.92.054322
114. S. Abrahamyan, Z. Ahmed, H. Albataineh et al., Measurement of the neutron radius of ^{208}Pb through parity violation in electron scattering. Phys. Rev. Lett. **108**, 112502 (2012). https://doi.org/10.1103/PhysRevLett.108.112502
115. C. Tarbert, D. Watts, D. Glazier et al., Neutron skin of ^{208}Pb from coherent pion photoproduction. Phys. Rev. Lett. **112**, 242502 (2014). https://doi.org/10.1103/PhysRevLett.112.242502
116. W. Horiuchi, S. Ebata, K. Iida, Neutron-skin thickness determines the surface tension of a compressible nuclear droplet. Phys. Rev. C **96**, 035804 (2017). https://doi.org/10.1103/PhysRevC.96.035804
117. E. Yüksel, E. Khan, K. Bozkurt et al., Effect of temperature on the effective mass and the neutron skin of nuclei. Eur. Phys. J. A **50**, 160 (2014). https://doi.org/10.1140/epja/i2014-14160-4
118. B. Brown, Mirror charge radii and the neutron equation of state. Phys. Rev. Lett. **119**, 122502 (2017). https://doi.org/10.1103/PhysRevLett.119.122502
119. J.J. Yang, J. Piekarewicz, Difference in proton radii of mirror nuclei as a possible surrogate for the neutron skin. Phys. Rev. C **97**, 014314 (2018). https://doi.org/10.1103/PhysRevC.97.014314
120. P. Reinhard, W. Nazarewicz, Information content of the differences in the charge radii of mirror nuclei. Phys. Rev. C **105**, L021301 (2022). https://doi.org/10.1103/PhysRevC.105.L021301

121. Y.N. Huang, Z.Z. Li, Y.F. Niu, Correlation between the difference of charge radii in mirror nuclei and the slope parameter of the symmetry energy. Phys. Rev. C **107**, 034319 (2023). https://doi.org/10.1103/PhysRevC.107.034319
122. M.Q. Ding, P. Su, D.Q. Fang et al., Investigation of the relationship between mirror proton radii and neutron-skin thickness. Chin. Phys. C **47**, 094101 (2023). https://doi.org/10.1088/1674-1137/ace680
123. T. Yamaguchi, M. Fukuda, S. Fukuda et al., Energy-dependent charge-changing cross sections and proton distribution of ^{28}Si. Phys. Rev. C **82**, 014609 (2010). https://doi.org/10.1103/PhysRevC.82.014609
124. T. Yamaguchi, I. Hachiuma, A. Kitagawa et al., Scaling of charge-changing interaction cross sections and point-proton radii of neutron-rich carbon isotopes. Phys. Rev. Lett. **107**, 032502 (2011). https://doi.org/10.1103/PhysRevLett.107.032502
125. A. Ozawa, T. Moriguchi, T. Ohtsubo et al., Charge-changing cross sections of ^{30}Ne, ^{32,33}Na with a proton target. Phys. Rev. C **89**, 044602 (2014). https://doi.org/10.1103/PhysRevC.89.044602
126. X.F. Li, D.Q. Fang, Y.G. Ma, Determination of the neutron skin thickness from interaction cross section and charge-changing cross section for B, C, N, O, F isotopes. Nucl. Sci. Tech. **27**, 71 (2016). https://doi.org/10.1007/s41365-016-0064-z
127. J.Y. Xu, Z.Z. Li, B.H. Sun et al., Constraining equation of state of nuclear matter by charge-changing cross section measurements of mirror nuclei. Phys. Lett. B **833**, 137333 (2022). https://doi.org/10.1016/j.physletb.2022.137333
128. P. Reinhard, A. Umar, P. Stevenson et al., Sensitivity of the fusion cross section to the density dependence of the symmetry energy. Phys. Rev. C **93**, 044618 (2016). https://doi.org/10.1103/PhysRevC.93.044618
129. S. Tagami, T. Wakasa, J. Matsui et al., Neutron skin thickness of ^{208}Pb determined from the reaction cross section for proton scattering. Phys. Rev. C **104**, 024606 (2021). https://doi.org/10.1103/PhysRevC.104.024606
130. F. Colomer, P. Capel, M. Ferretti et al., Theoretical analysis of the extraction of neutron skin thickness from coherent π^0 photoproduction off nuclei. Phys. Rev. C **106**, 044318 (2022). https://doi.org/10.1103/PhysRevC.106.044318
131. T. Wakasa, S. Tagami, J. Matsui et al., Reaction cross section of proton scattering consistent with PREX-II. Results Phys. **29**, 104749 (2021). https://doi.org/10.1016/j.rinp.2021.104749
132. J. Lattimer, Constraints on nuclear symmetry energy parameters. Particles **6**, 30–56 (2023). https://doi.org/10.3390/particles6010003
133. E. Thein, N. Lwin, K. Hagino, Transition from subbarrier to deep-subbarrier regimes in heavy-ion fusion reactions. Phys. Rev. C **85**, 057602 (2012). https://doi.org/10.1103/PhysRevC.85.057602
134. K. Hagino, *Sub-Barrier Fusion Reactions*. (Springer Nature, Singapore, 2020) https://doi.org/10.1007/978-981-15-8818-1_9-1
135. T. Ghosh, Sangeeta, G. Saxena et al., Impact of density dependence of symmetry energy on astrophysical S-factor for heavy-ion fusion reactions. Eur. Phys. J. A **59**, 266 (2023). https://doi.org/10.1140/epja/s10050-023-01173-7
136. J.H. Chen, D. Keane, Y.G. Ma et al., Antinuclei in heavy-ion collisions. Phys. Rep. **760**, 1–39 (2018). https://doi.org/10.1016/j.physrep.2018.07.002
137. M. Abdallah et al., Pattern of global spin alignment of ϕ and K^{*0} mesons in heavy-ion collisions. Nature **614**, 244 (2023). https://doi.org/10.1038/s41586-022-05557-5
138. K.J. Sun, R. Wang, C.M. Ko et al., Unveiling the dynamics of little-bang nucleosynthesis. Nat. Commun. **15**, 1074 (2024). https://doi.org/10.1038/s41467-024-45474-x
139. Y. Zhang, D.W. Zhang, X.F. Luo, Experimental study of the QCD phase diagram in relativistic heavy-ion collisions. Nucl. Tech. (in Chinese) **46**, 040001 (2023). https://doi.org/10.11889/j.0253-3219.2023.hjs.46.040001
140. K.J. Sun, L.W. Chen, C.M. Ko et al., Light nuclei production and QCD phase transition in heavy-ion collisions. Nucl. Tech. (in Chinese) **46**, 040012 (2023). https://doi.org/10.11889/j.0253-3219.2023.hjs.46.040012
141. F.P. Li, L.G. Pang, X.N. Wang, Application of machine learning to the study of QCD transition in heavy ion collisions. Nucl. Tech. (in Chinese) **46**, 040014 (2023). https://doi.org/10.11889/j.0253-3219.2023.hjs.46.040014
142. J.H. Gao, X.G. Huang, Z.T. Liang et al., Spin-orbital coupling in strong interaction and global spin polarization. Acta Phys. Sin. (in Chinese) **72**, 072501 (2023). https://doi.org/10.7498/aps.72.20230102
143. X.L. Zhao, G.L. Ma, Y.G. Ma, Electromagnetic field effects and anomalous chiral phenomena in heavy-ion collisions at intermediate and high energy. Acta Phys. Sin. (in Chinese) **72**, 112502 (2023). https://doi.org/10.7498/aps.72.20230245
144. W.B. He, Y.G. Ma, L.G. Pang et al., High-energy nuclear physics meets machine learning. Nucl. Sci. Tech. **34**, 88 (2023). https://doi.org/10.1007/s41365-023-01233-z
145. Y.G. Ma, L.G. Pang, R. Wang et al., Phase transition study meets machine learning. Chin. Phys. Lett. **40**, 122101 (2023). https://doi.org/10.1088/0256-307X/40/12/122101
146. X.N. Wang, Vector meson spin alignment by the strong force field. Nucl. Sci. Tech. **34**, 15 (2023). https://doi.org/10.1007/s41365-023-01166-7
147. Y.G. Ma, New type of double-slit interference experiment at fermi scale. Nucl. Sci. Tech. **34**, 16 (2023). https://doi.org/10.1007/s41365-023-01167-6
148. Y.G. Ma, S. Zhang, *Influence of Nuclear Structure in Relativistic Heavy-Ion Collisions*. (Springer Nature, Singapore, 2020) https://doi.org/10.1007/978-981-15-8818-1_5-1
149. H.J. Xu, Constraints on neutron skin thickness and nuclear deformations using relativistic heavy-ion collisions from STAR. Acta Phys. Polon. Supp. **16**, 1-A30 (2023). https://doi.org/10.5506/APhysPolBSupp.16.1-A30
150. M. Abdallah, B. Aboona, J. Adam et al., Search for the chiral magnetic effect with isobar collisions at $\sqrt{s_{\rm NN}} = 200$ GeV by the STAR collaboration at the BNL relativistic heavy ion collider. Phys. Rev. C **105**, 014901 (2022). https://doi.org/10.1103/PhysRevC.105.014901
151. F. Li, Y.G. Ma, S. Zhang et al., Impact of nuclear structure on the background in the chiral magnetic effect in $^{96}_{44}$Ru +$^{96}_{44}$ Ru and $^{96}_{40}$Zr +$^{96}_{40}$ Zr collisions at $\sqrt{s_{\rm NN}} = 7.7$–200 GeV from a multiphase transport model. Phys. Rev. C **106**, 014906 (2022). https://doi.org/10.1103/PhysRevC.106.014906
152. H.L. Li, H.J. Xu, Y. Zhou et al., Probing the neutron skin with ultrarelativistic isobaric collisions. Phys. Rev. Lett. **125**, 222301 (2020). https://doi.org/10.1103/PhysRevLett.125.222301
153. L.M. Liu, C.J. Zhang, J. Zhou et al., Probing neutron-skin thickness with free spectator neutrons in ultracentral high-energy isobaric collisions. Phys. Lett. B **834**, 137441 (2022). https://doi.org/10.1016/j.physletb.2022.137441
154. L.M. Liu, C.J. Zhang, J. Xu et al., Free spectator nucleons in ultracentral relativistic heavy-ion collisions as a probe of neutron skin. Phys. Rev. C **106**, 034913 (2022). https://doi.org/10.1103/PhysRevC.106.034913
155. H.J. Xu, W.B. Zhao, H.L. Li et al., Probing nuclear structure with mean transverse momentum in relativistic isobar collisions. Phys. Rev. C **108**, L011902 (2023). https://doi.org/10.1103/PhysRevC.108.L011902

156. H.J. Xu, H.L. Li, Y. Zhou et al., Measuring neutron skin by grazing isobaric collisions. Phys. Rev. C **105**, L011901 (2022). https://doi.org/10.1103/PhysRevC.105.L011901
157. G. Giacalone, G. Nijs, W. van der Schee, Determination of the neutron skin of ^{208}Pb from ultrarelativistic nuclear collisions. Phys. Rev. Lett. **131**, 202302 (2023). https://doi.org/10.1103/PhysRevLett.131.2023027
158. M. Abdallah et al., Tomography of ultrarelativistic nuclei with polarized photon-gluon collisions. Sci. Adv. **9**, eabq3903 (2023). https://doi.org/10.1126/sciadv.abq3903
159. Imaging shapes of atomic nuclei in high-energy nuclear collisions. arXiv 2401.06625 (2024). https://doi.org/10.48550/arXiv.2401.06625
160. R. Casten, Scientific opportunities with an advanced isol facility. Nucl. Phys. News **8**, 25–26 (1998). https://doi.org/10.1080/10506899809410876
161. Y. Blumenfeld, T. Nilsson, P.V. Duppen, Facilities and methods for radioactive ion beam production. Physica Scripta **2013**, 014023 (2013). https://doi.org/10.1088/0031-8949/2013/T152/014023
162. I. Tanihata, H. Hamagaki, O. Hashimoto et al., Measurements of interaction cross sections and nuclear radii in the light *p*-shell region. Phys. Rev. Lett. **55**, 2676–2679 (1985). https://doi.org/10.1103/PhysRevLett.55.2676
163. I. Tanihata, H. Hamagaki, O. Hashimoto et al., Measurements of interaction cross sections and radii of he isotopes. Phys. Lett. B **160**, 380–384 (1985). https://doi.org/10.1016/0370-2693(85)90005-X
164. S. Kox, A. Gamp, C. Perrin et al., Trends of total reaction cross sections for heavy ion collisions in the intermediate energy range. Phys. Rev. C **35**, 1678–1691 (1987). https://doi.org/10.1103/PhysRevC.35.1678
165. W.Q. Shen, B. Wang, J. Feng et al., Total reaction cross section for heavy-ion collisions and its relation to the neutron excess degree of freedom. Nucl. Phys. A **491**, 130–146 (1989). https://doi.org/10.1016/0375-9474(89)90209-1
166. S. Charagi, S. Gupta, Coulomb-modified glauber model description of heavy-ion reaction cross sections. Phys. Rev. C **41**, 1610–1618 (1990). https://doi.org/10.1103/PhysRevC.41.1610
167. Y.G. Ma, W.Q. Shen, J. Feng et al., A novel path to study the total reaction cross sections. Phys. Lett. B **302**, 386–389 (1993). https://doi.org/10.1016/0370-2693(93)90414-D
168. Y.G. Ma, W.Q. Shen, J. Feng et al., Study of the total reaction cross section via the reaction dynamical model. Phys. Rev. C **48**, 850–856 (1993). https://doi.org/10.1103/PhysRevC.48.850
169. D.Q. Fang, T. Yamaguchi, T. Zheng et al., One-neutron halo structure in ^{15}C. Phys. Rev. C **69**, 034613 (2004). https://doi.org/10.1103/PhysRevC.69.034613
170. D.Q. Fang, W. Guo, C.W. Ma et al., Examining the exotic structure of the proton-rich nucleus ^{23}Al. Phys. Rev. C **76**, 031601 (2007). https://doi.org/10.1103/PhysRevC.76.031601
171. N. Orr, N. Anantaraman, S. Austin et al., Momentum distributions of ^{9}Li fragments from the breakup of ^{11}Li and the neutron halo. Phys. Rev. C **51**, 3116–3126 (1995). https://doi.org/10.1103/PhysRevC.51.3116
172. N. Orr, Fragment momentum distributions and the halo. Nucl. Phys. A **616**, 155–168 (1997). https://doi.org/10.1016/S0375-9474(97)00085-7
173. M. Zahar, M. Belbot, J. Kolata et al., Momentum distributions for ^{12,14}Be fragmentation. Phys. Rev. C **48**, R1484–R1487 (1993). https://doi.org/10.1103/PhysRevC.48.R1484
174. D. Adhikari, H. Albataineh, D. Androic et al., Accurate determination of the neutron skin thickness of ^{208}Pb through parity-violation in electron scattering. Phys. Rev. Lett. **126**, 172502 (2021). https://doi.org/10.1103/PhysRevLett.126.172502
175. D. Adhikari, H. Albataineh, D. Androic et al., Precision determination of the neutral weak form factor of ^{48}Ca. Phys. Rev. Lett. **129**, 042501 (2022). https://doi.org/10.1103/PhysRevLett.129.042501
176. B. Reed, F. Fattoyev, C. Horowitz et al., Implications of PREX-2 on the equation of state of neutron-rich matter. Phys. Rev. Lett. **126**, 172503 (2021). https://doi.org/10.1103/PhysRevLett.126.172503
177. S. Tagami, T. Wakasa, M. Yahiro, Slope parameters determined from crex and prex2. Results Phys. **43**, 106037 (2022). https://doi.org/10.1016/j.rinp.2022.106037
178. Z. Zhang, L.W. Chen, Bayesian inference of the symmetry energy and the neutron skin in ^{48}Ca and ^{208}Pb from CREX and PREX-2. Phys. Rev. C **108**, 024317 (2023). https://doi.org/10.1103/PhysRevC.108.024317